The Astronomical Journal, 172:296 (19pp), 2026 December https://doi.org/10.3847/1538-3881/aeb1d6
© 2026. The Author(s). Published by the American Astronomical Society.
OPEN ACCESS

Kinematic and Dynamical Properties of Solar-neighborhood White Dwarfs from SDSS Data Release 19 and Gaia Data Release 3

Ozcan Caliskan[1], Selçuk Bilir[2], and Mukremin Kilic[3]
[1] Programme of Astronomy and Space Sciences, Institute of Graduate Studies in Science, Istanbul University, 34116 Istanbul, Türkiye; caliskanozcan@hotmail.com
[2] Department of Astronomy and Space Sciences, Faculty of Science, Istanbul University, 34119 Beyazıt, Istanbul, Türkiye
[3] Homer L. Dodge Department of Physics and Astronomy, University of Oklahoma, 440 West Brooks Street, Norman, OK 73019, USA
Received 2026 August 19; revised 2026 October 6; accepted 2026 October 6; published 2026 November 2

Abstract

We present a comprehensive kinematic and dynamical analysis of 5837 white dwarfs with hydrogen-rich atmospheres, SDSS DR19 spectroscopy, and Gaia Data Release 3 astrometry. Using complementary spatial distributions, kinematic properties, and orbital parameters, we show that the sample is overwhelmingly dominated by the thin disk, with only minor contributions from the thick disk and the halo. Velocity dispersions and orbital eccentricities increase systematically from the thin disk to the halo, reflecting progressively hotter Galactic populations. Total stellar ages available for 4829 white dwarfs reveal a clear age–velocity dispersion relation with power-law indices of 0.06–0.17, confirming that white dwarfs preserve the secular dynamical heating history of the Galactic disk. We derive a thin-disk scale height of 123–229 pc and radial scale length of 3.2–3.5 kpc, while the thick disk has a scale height of 865 pc and contributes approximately 6%–7% of the local stellar density. Reconstructed birth radii indicate that changes in the guiding radii represent an important component of the present-day radial redistribution of nearby white dwarfs, although the relative contributions of radial migration and orbital blurring cannot be uniquely separated from these displacement measures. These results establish white dwarfs as powerful tracers of the kinematic, dynamical, and structural evolution of the Milky Way.

Unified Astronomy Thesaurus concepts: White dwarf stars (1799); Galaxy structure (622); Galaxy kinematics (602); Solar neighborhood (1509)

Materials only available in the online version of record: machine-readable table

1. Introduction

White dwarfs (WDs) constitute the final evolutionary products of nearly all low- and intermediate-mass stars and are therefore among the most abundant stellar remnants in the Milky Way. Their predictable cooling evolution (L. Mestel 1952) and relatively simple internal structure make them fundamental laboratories for studying stellar evolution and the Galactic structure (G. Fontaine et al. 2001; L. G. Althaus et al. 2010). Because WDs cool over Gyr timescales, their present-day kinematic properties retain important signatures of the dynamical heating, radial migration, and secular evolution processes that have shaped the Galactic disk throughout its history (D. E. Winget et al. 1987; J. Liebert et al. 1988; P.-E. Tremblay et al. 2014). Their kinematics and Galactic orbits provide valuable constraints on the age distribution, dynamical evolution, and the structure of the Milky Way disk and halo (E.-M. Pauli et al. 2006; B. Anguiano et al. 2017; M. Kilic et al. 2017; R. Raddi et al. 2022).

Over the last quarter century, large-scale photometric, astrometric, and spectroscopic surveys, particularly the Sloan Digital Sky Survey (SDSS; D. G. York et al. 2000) and the Gaia mission (Gaia Collaboration et al. 2018), have revealed that the Galactic disk exhibits a rich and dynamically complex structure shaped by processes such as secular heating, radial migration, spiral arm perturbations, bar resonances, and interactions with satellite galaxies (e.g., J. A. Sellwood & J. J. Binney 2002; R. Schönrich & J. Binney 2009; I. Minchev & B. Famaey 2010; T. Antoja et al. 2018; A. Helmi et al. 2018). WDs constitute particularly valuable kinematic tracers as they represent stellar populations spanning a wide range of ages (E.-M. Pauli et al. 2006; N. P. Gentile Fusillo et al. 2019; F. M. Jiménez-Esteban et al. 2018). Specifically, the observed relation between the stellar age and the space-velocity dispersion provides one of the strongest empirical constraints on the models of Galactic disk heating and dynamical evolution (R. Wielen 1977; M. Aumer & J. J. Binney 2009; Y.-S. Ting & H.-W. Rix 2019). S. Cheng et al. (2019) used a photometrically selected sample of high-mass WDs from Gaia Data Release 2 (DR2; Gaia Collaboration et al. 2018) to model their transverse-velocity distributions as a function of age, and demonstrate the value of WD kinematics as an independent constraint on stellar ages.

Before Gaia, kinematic investigations of WD populations were generally restricted to relatively small and heterogeneous samples due to the limited availability of accurate trigonometric parallaxes, proper motions, and radial velocities. Significant progress was made with the ESO Supernovae Type Ia Progenitor Survey (SPY), which provided high-resolution spectroscopic observations and accurate radial velocity measurements for several hundred WDs with hydrogen-rich atmospheres (DA WDs; e.g., R. Napiwotzki et al. 2001; E.-M. Pauli et al. 2003; C. A. Karl et al. 2005). By combining spectroscopic radial velocities with proper motions and spectroscopic parallax estimates, these studies enabled a more reliable separation of thin-disk, thick-disk, and halo populations based on their Galactic space motions and orbital parameters (E.-M. Pauli et al. 2006).

Original content from this work may be used under the terms of the Creative Commons Attribution 4.0 licence. Any further distribution of this work must maintain attribution to the author(s) and the title of the work, journal citation and DOI.

B. Anguiano et al. (2017) significantly expanded upon this work by using the DA WD sample from the SDSS DR12: they confirmed the existence of a mean Galactocentric radial velocity gradient, and found evidence of an additional source of heating in the disk. The SPY and the SDSS DR12 samples highlighted the importance of full three-dimensional kinematic information for distinguishing Galactic populations and constraining the evolutionary history of WDs in the solar neighborhood. Nevertheless, pre-Gaia investigations remained limited by small sample sizes, selection biases, or incomplete phase-space information.

S. Torres et al. (2019) applied a random forest algorithm trained on population-synthesis models to distinguish thin-disk, thick-disk, and halo stars in the Gaia DR2 100 pc WD sample. Their analysis demonstrated that probabilistic classification based on astrometric and photometric information provides a complementary approach to conventional kinematic criteria for separating Galactic WD populations.

Recently, R. Raddi et al. (2022) took advantage of the Gaia Early Data Release 3 (Gaia EDR3; Gaia Collaboration et al. 2021) astrometry to revisit the SPY and SDSS DR12 DA WD samples. They also included common proper-motion pairs of WDs with nondegenerate companions, where the radial velocity or metallicity of the companion is constrained from spectroscopy. R. Raddi et al. (2022) found that their sample is dominated (90%–95%) by thin-disk stars, with negligible contribution from the halo. Studying the age–velocity dispersion relation (AVR) for the disk, they found evidence of dynamical heating and saturation after 4–6 Gyr, which could be driven by giant molecular clouds, the spiral structure, Galactic bar perturbations, and merger events (C. G. Lacey 1984; R. De Simone et al. 2004; R. J. J. Grand et al. 2016). However, the relative contributions of these processes remain a matter of active debate. More recently, A. Swan et al. (2026) presented a kinematic analysis of the Dark Energy Spectroscopic Instrument (DESI) Data Release 1 (DR1) WD sample (see also M. Kilic et al. 2026a, 2026b; L. L. Amorim et al. 2026) combining spectroscopic radial velocities and distance estimates with Gaia proper motions. Using a Gaussian mixture model applied to the three-dimensional velocity distributions, they found that only about 1% of the stars have a probability $> 50\%$ of being a halo star, indicating that the DESI sample is also dominated by the Galactic disk.

The SDSS WD sample has grown significantly since DR12 (S. O. Kepler et al. 2019, 2021; N. R. Crumpler et al. 2025). In this study, we investigate the kinematic properties of a sample of more than 5800 WDs by combining Gaia astrometric data with the latest SDSS spectroscopic measurements. Using this statistically significant sample, we analyze the Galactic velocity distributions and examine the kinematic behavior of the WD population in the context of Galactic disk evolution. The paper is organized as follows. In Section 2, we describe the sample selection and data used in this work. Section 3 presents the methods employed to derive the kinematic and Galactic orbital parameters. The results of the analyses of the spatial distribution, kinematics, and Galactic orbital parameters of the WDs are presented in Section 4, while Section 5 summarizes the main findings and discusses their implications. We conclude in Section 6.

2. Data

Our study is based on the DA WD catalog of N. R. Crumpler et al. (2025), which provides a large and comprehensive sample of spectroscopically confirmed WDs. This dataset encompasses observations from both Data Release 19 (DR19) of the ongoing SDSS-V survey (8545 DAs) and previous generations of the SDSS (19,257 DAs), resulting in a sample of 26,041 unique DA WDs, after accounting for an overlap of 1761 sources observed across both SDSS-V DR19 and earlier SDSS generations. This sample offers a homogeneous spectroscopic dataset optimized for kinematic studies, delivering precise radial velocity measurements, spectroscopic effective temperatures ($T_{\rm eff}$), and surface gravities ($\log g$) for hydrogen atmosphere WDs. In addition, high-precision proper motions and trigonometric parallaxes from Gaia DR3, and geometric distance estimates from C. A. L. Bailer-Jones et al. (2021) enable a full six-dimensional phase-space characterization of this WD sample.

Table 1
Quality Cuts for Our White Dwarf Catalog

Criterion	Explanation
$\sigma_d/d \leqslant 0.20$	Distance uncertainty limit
$\sigma_{V\rm rad} \leqslant 15$ km s^{-1}	Radial velocity uncertainty limit
`binary_flag` $= 0$	Exclusion of binaries
SNR $\geqslant 10$	Minimum SNR
RUWE $\leqslant 1.4$	Gaia astrometric quality cut
Final sample: 5894 WDs	

We construct our kinematic sample by applying a series of quality cuts, given in Table 1, to ensure reliable astrometric and spectroscopic measurements. We retain only sources with relative distance uncertainties below 20%, radial velocity uncertainties smaller than 15 km s^{-1}, and signal-to-noise ratio (SNR) $\geqslant 10$ spectra. We further exclude binary candidates by requiring `binary_flag` $= 0$ and imposing the Gaia astrometric quality cut RUWE $\leqslant 1.4$. These selection criteria reduce the sample to 5894 WDs.

3. Methods

In this section, we present a unified analysis framework covering WD kinematics, Galactic orbital properties, population classification, age estimation, and Galactic structure. First, space-velocity components are computed from astrometric data and available radial velocities. Radial velocities of WDs require special treatment because the measured spectroscopic velocities include both the intrinsic stellar motion and the gravitational redshift produced by the strong gravitational potential at the stellar surface (e.g., R. E. Falcon et al. 2010). Therefore, to derive reliable three-dimensional kinematics, the observed radial velocities were corrected for gravitational redshift before computing the Galactic space motions.

The effective temperatures ($T_{\rm eff}$) and surface gravities ($\log g$) adopted from N. R. Crumpler et al. (2025) were used as input to `wdwarfdate` (R. Kiman et al. 2022) to infer the WD masses. The corresponding stellar radii were then derived from the relation $R_{\rm WD} = \sqrt{(GM_{\rm WD}/g)}$. Using these internally consistent mass and radius estimates, the gravitational-redshift contribution was calculated individually for each WD as $V_{\rm gr} = (GM_{\rm WD})/(R_{\rm WD}c) = 0.635(M_{\rm WD}/M_{\odot})/(R_{\rm WD}/R_{\odot})$ km s^{-1}, and was subtracted from the measured apparent spectroscopic radial velocity, such that $V_{\rm rad} = V_{\rm rad,\,obs} - V_{\rm gr}$. Thus, the masses and radii used in the gravitational-redshift correction were not adopted directly from N. R. Crumpler et al. (2025); rather, the WD masses were inferred with `wdwarfdate` from

the spectroscopic parameters of N. R. Crumpler et al. (2025), and the radii were subsequently derived from the corresponding masses and surface gravities. The corrected radial velocities were then used to calculate the Galactic space-velocity components. From these, Galactic orbital parameters such as apogalactic and perigalactic distances, eccentricity, and maximum vertical height from the Galactic plane are derived. The sample is then classified into thin-disk, thick-disk, and halo populations based on probabilistic kinematic criteria and Galactic orbital parameters. Finally, the Jeans equations are applied to the full sample to derive the radial and vertical scale lengths of the Galactic disk.

3.1. White Dwarf Age Determination

Total stellar ages and progenitor masses were determined with the Bayesian framework implemented in the `wdwarfdate` package (R. Kiman et al. 2022). For our DA WD sample, we adopted the thick H atmosphere cooling sequences of A. Bédard et al. (2020), the MESA Isochrones and Stellar Tracks (MIST)-based initial–final mass relation (IFMR) of J. D. Cummings et al. (2018), and the MIST evolution models (J. Choi et al. 2016; A. Dotter 2016) to determine the progenitor lifetimes. The progenitor models were evaluated at solar metallicity ([Fe/H] = 0 dex) with no rotation ($V/V_{\rm crit} = 0$). The measured $T_{\rm eff}$ and $\log g$, together with their uncertainties, were supplied to `wdwarfdate`, which evaluates their posterior distributions and derives the WD mass and cooling age ($t_{\rm cool}$), the progenitor mass and lifetime ($t_{\rm MS}$), and the total stellar age ($t_{\rm tot} = t_{\rm cool} + t_{\rm MS}$). The quoted values are the posterior medians, while the lower and upper uncertainties are the 16th and 84th percentiles, respectively. The Bayesian calculation also accounts for the intrinsic scatter in the adopted IFMR.

We adopted solar-metallicity progenitor models uniformly for the full sample. The metallicities of the progenitor stars cannot be measured directly for isolated WDs, and assigning a mean metallicity according to kinematic population membership would introduce an additional model-dependent assumption. Nevertheless, progenitor metallicity affects both the pre-WD evolutionary lifetime and, to some extent, the IFMR (e.g., A. D. Romero et al. 2015). Therefore, the total ages derived here should be interpreted within the adopted solar-metallicity framework, particularly for thick-disk and halo WDs whose progenitors are expected, on average, to be more metal poor. This metallicity dependence represents an additional systematic uncertainty in the total ages that is not included in the quoted statistical uncertainties.

3.2. Space Velocities

We computed the three-dimensional Galactic space-velocity components (U, V, W) following the general matrix formalism of D. R. H. Johnson & D. R. Soderblom (1987), while adopting the updated International Celestial Reference System–based equatorial-to-Galactic transformation used in the Gaia astrometric framework (ESA 1997; Gaia Collaboration et al. 2021). This analysis requires four input parameters: the equatorial coordinates (α, δ), proper-motion components ($\mu_\alpha \cos\delta$, μ_δ), geometric distances (d), and radial velocities ($V_{\rm rad}$). The uncertainties in the Galactic space-velocity components were calculated individually for each WD following the error-propagation formalism of D. R. H. Johnson & D. R. Soderblom (1987) and the observational uncertainties in proper motion, geometric distance, and radial velocity. For the geometric distances adopted from C. A. L. Bailer-Jones et al. (2021), the catalog-reported distance uncertainties were used directly, without any additional transformation or reestimation of the distance posterior. The Gaia astrometric covariance terms and the possible asymmetry of the individual distance posteriors were not explicitly incorporated into this analytic error propagation. In this study, we adopt a left-handed Galactic coordinate system, where U is positive toward the Galactic center ($\ell = 0^\circ$, $b = 0^\circ$), V is positive in the direction of Galactic rotation ($\ell = 90^\circ$, $b = 0^\circ$), and W is positive toward the north Galactic pole ($\ell = 0^\circ$, $b = 90^\circ$).

Since the astrometric and spectroscopic observables are measured in the heliocentric reference frame, the derived Galactic space-velocity components are affected by the local effects of Galactic differential rotation. To account for this effect, corrections (dU and dV) were applied to the initially calculated velocity components following the formalism of D. Mihalas & J. Binney (1981) using the following relations:

$$\begin{aligned} dU &= V_{\rm rad}\cos\ell - V_{\rm t}\sin\ell, \\ dV &= V_{\rm rad}\sin\ell - V_{\rm t}\cos\ell, \end{aligned} \tag{1}$$

where $V_{\rm rad}$ and $V_{\rm t}$ denote the Galactic radial and tangential velocity components, respectively, and ℓ represents the Galactic longitude. First-order effects of Galactic rotation are confined to the in-plane velocity components (U and V), while the vertical component W remains unaffected, since no significant coupling exists between vertical motions and planar differential rotation in the solar neighborhood (S. Bilir et al. 2012; B. Coşkunoğlu et al. 2012). The corrections accounting for Galactic differential rotation are applied to the observed velocity components in the Galactic plane and are evaluated within the standard linear approximation. The corresponding kinematic corrections are expressed in terms of the radial and tangential components of the Galactic rotation field in the plane, commonly formulated via the Oort constants as

$$\begin{aligned} V_{\rm t} &= r \times (A \times \cos 2\ell + B), \\ V_{\rm rad} &= A \times d \times \sin 2\ell, \end{aligned} \tag{2}$$

where A and B are the Oort constants, for which we adopt $A = 15.3 \pm 0.4\,{\rm km\,s^{-1}\,kpc^{-1}}$ and $B = -11.9 \pm 0.4\,{\rm km\,s^{-1}\,kpc^{-1}}$, as measured from Gaia DR1/TGAS data (J. Bovy 2017). The parameter r defines the projection distance of the star onto the Galactic plane, given by $r = d \times \cos b$, where d is the heliocentric distance in kpc.

Finally, to eliminate heliocentric bias and project the motion onto the local standard of rest (LSR) frame, we correct for the peculiar motion of the Sun. The absolute, corrected space-velocity components relative to the LSR ($U_{\rm LSR}$, $V_{\rm LSR}$, and $W_{\rm LSR}$) are derived via linear translations:

$$\begin{aligned} U_{\rm LSR} &= U - dU + U_\odot, \\ V_{\rm LSR}, &= V - dV + V_\odot, \\ W_{\rm LSR} &= W + W_\odot, \end{aligned} \tag{3}$$

where we adopt the solar-motion vector ($U_\odot$, $V_\odot$, $W_\odot$) = $(8.83 \pm 0.24, 14.19 \pm 0.34, 6.57 \pm 0.21)\,{\rm km\,s^{-1}}$ (B. Coşkunoğlu et al. 2011). For the subsequent orbit calculations with `galpy`, the solar-motion vector was transformed to the native

galpy convention, for which the input is specified as $[-U_\odot, V_\odot, W_\odot]$. Accordingly, we adopted $(-8.83, 14.19, 6.57)\,\mathrm{km\,s^{-1}}$ when initializing the orbits, ensuring consistency between the heliocentric velocity convention adopted above and the Galactocentric orbit calculations. The total space velocity relative to the LSR is then calculated as $S_{\rm LSR} = \sqrt{U_{\rm LSR}^2 + V_{\rm LSR}^2 + W_{\rm LSR}^2}$. To ensure a robust kinematic analysis, objects with uncertainties in $S_{\rm LSR}$ exceeding 20 km s^{-1} were excluded from the sample. This quality criterion removed 57 WDs, yielding a final kinematic sample of 5837 objects used throughout the remainder of this study.

We further derive the Galactocentric velocity components in a cylindrical coordinate system with V_R, V_ϕ, and V_Z, where V_Z is equivalent to W, and

$$V_R = \frac{1}{R}[X_{\rm gc}\cdot U_{\rm LSR} + Y_{\rm gc}\cdot (V_{\rm LSR} + V_{\rm rot})], \quad (4)$$

$$V_\phi = \frac{1}{R}[X_{\rm gc}\cdot (V_{\rm LSR} + V_{\rm rot}) - Y_{\rm gc}\cdot U_{\rm LSR}], \quad (5)$$

and $R = \sqrt{X_{\rm gc}^2 + Y_{\rm gc}^2}$ is the present-day Galactocentric cylindrical radius of each WD. We adopted a solar Galactocentric distance of $R_0 = 8$ kpc and a local circular velocity of $V_{\rm rot} = 220$ km s^{-1} (J. Bovy & S. Tremaine 2012; J. Bovy 2015). We calculate the position of each object in Galactocentric Cartesian coordinates ($X_{\rm gc}$, $Y_{\rm gc}$, $Z_{\rm gc}$):[4]

$$\begin{aligned} X_{\rm gc} &= d\cos b\cos l - X_\odot,\\ Y_{\rm gc} &= d\cos b\sin l,\\ Z_{\rm gc} &= d\sin b. \end{aligned} \quad (6)$$

3.3. Galactic Orbital Parameters

We used galpy (J. Bovy 2015) to derive the Galactic orbital parameters, adopting its standard axisymmetric MWPotential2014 model. The potential consists of an exponentially truncated power-law bulge, a Miyamoto–Nagai disk (M. Miyamoto & R. Nagai 1975), and a Navarro–Frenk–White (NFW) dark-matter halo (J. F. Navarro et al. 1996). We adopted the standard MWPotential2014 scaling of $R_0 = 8$ kpc and $V_0 = 220$ km s^{-1}. The bulge has a power-law index of 1.8 and a cutoff radius of 1.9 kpc; the disk has radial and vertical scale parameters of $a = 3.0$ kpc and $b = 0.28$ kpc, respectively; and the NFW halo has a scale radius of $r_s = 16$ kpc. The bulge, disk, and halo components are normalized to contribute 0.05, 0.60, and 0.35, respectively, to the radial force at R_0 (J. Bovy 2015). We further assumed that the Sun lies 27 ± 4 pc above the Galactic plane (B. Chen et al. 2001).

Each orbit was integrated backward for 10 Gyr with a time step of 1 Myr. From the resulting trajectories, we derived the perigalactic ($R_{\rm peri}$) and apogalactic ($R_{\rm apo}$) distances, the maximum vertical distance from the Galactic plane ($Z_{\rm max}$), the orbital eccentricity (e), the guiding radius ($R_{\rm g}$), and the orbital period ($P_{\rm orb}$).

[4] The heliocentric space velocities are expressed in the right-handed convention defined above, whereas the orbital calculations follow the native left-handed Galactocentric convention of galpy.

3.4. Kinematic Population Analysis

We determine the Galactic population membership of each WD based on the kinematic classification scheme of T. Bensby et al. (2003, 2005), which assumes that the Galactic space-velocity components of the thin-disk ("*D*"), thick-disk ("*TD*"), and halo ("*H*") populations follow Gaussian distributions characterized by distinct velocity dispersions and asymmetric drift velocities. For a given population i (D, TD, and H) the probability distribution (P_i) is

$$P_i(U, V, W) = k_i \exp\left[-\frac{U_{\rm LSR}^2}{2\sigma_{U,i}^2} - \frac{(V_{\rm LSR} - V_{{\rm asym},i})^2}{2\sigma_{V,i}^2} - \frac{W_{\rm LSR}^2}{2\sigma_{W,i}^2}\right], \quad (7)$$

where σ_U, σ_V, and σ_W are the characteristic velocity dispersions, $V_{\rm asym}$ is the asymmetric drift velocity, and k_i is the normalization constant:

$$k_i = \frac{1}{(2\pi)^{3/2}\sigma_U\sigma_V\sigma_W}. \quad (8)$$

Following T. Bensby et al. (2005), the characteristic velocity dispersions (σ_U, σ_V, σ_W) are (35, 20, 16) km s^{-1} for the thin disk, (67, 38, 35) km s^{-1} for the thick disk, and (160, 90, 90) km s^{-1} for the halo. The corresponding asymmetric drift velocities, $V_{\rm asym}$, are -15, -46, and -220 km s^{-1}, respectively. Local stellar population fractions of $X_D = 0.9385$, $X_{TD} = 0.06$, and $X_H = 0.0015$ were adopted based on the estimates from R. Buser et al. (1999) and S. Bilir et al. (2008). The relative probabilities between populations were computed as

$$\frac{TD}{D} = \frac{X_{TD}}{X_D}\frac{P_{TD}}{P_D}, \qquad \frac{TD}{H} = \frac{X_{TD}}{X_H}\frac{P_{TD}}{P_H}, \quad (9)$$

where P_i denotes the probability associated with population i. We classify stars with $TD/D \leqslant 0.1$ as high-probability thin-disk members, and those with $TD/D > 10$ as high-probability thick-disk or halo stars. We identify objects with $0.1 < TD/D \leqslant 1$ and $1 < TD/D \leqslant 10$ as low-probability thin-disk and thick-disk members, respectively. For the population-based analyses presented in this study, the high- and low-probability thin-disk categories were combined, and WDs with $TD/D \leqslant 1$ were assigned to the thin-disk sample. Among the objects with $TD/D > 10$, those satisfying $TD/H > 1$ were classified as thick-disk members, whereas those with $TD/H \leqslant 1$ were assigned to the halo. Thus, the TD/H ratio explicitly distinguishes the thick-disk and halo populations within the kinematically hot ($TD/D > 10$) subsample. Objects with $1 < TD/D \leqslant 10$ were classified as transition objects and were therefore excluded from the final thin-disk, thick-disk, and halo samples.

3.5. Jeans Analysis of Radial and Vertical Disk Scales from White Dwarfs

Although WDs are intrinsically faint and therefore restricted to a relatively small volume in the solar neighborhood, their kinematics still encode information on the global dynamical properties of the Galactic disk. Thus, the observed velocity ellipsoids can be exploited within the Jeans formalism to obtain indirect constraints on the structural parameters of the thin- and thick-disk components (G. Kordopatis et al. 2011).

The geometric distances adopted from C. A. L. Bailer-Jones et al. (2021) are based on a direction-dependent Galactic distance prior. This prior does not directly set the disk scale lengths or scale heights derived here, because these quantities are inferred from the Jeans equations using the velocity moments and their spatial gradients rather than from a direct fit to the stellar distance distribution. Nevertheless, the adopted distances enter indirectly through the Galactocentric positions and tangential velocities, and therefore some residual dependence on the distance prior cannot be excluded. The effect is expected to be limited for our nearby sample, which has a median distance of 214 pc and is restricted to sources with relative distance uncertainties below 20%. In the following, we combine the derived velocity ellipsoids with the Jeans equations under the assumption of steady-state equilibrium to estimate the radial scale length (h_R) and the vertical scale height (h_Z). In cylindrical coordinates, the Jeans equations for the radial and vertical components are given by

$$v_c^2 - \bar{v_\phi}^2 = \sigma_{V_R}^2 \left(\frac{\sigma_{V_\phi}^2}{\sigma_{V_R}^2} - 1 - \frac{\partial \ln(\rho \sigma_{V_R}^2)}{\partial \ln R} - \frac{R}{\sigma_{V_R}^2} \frac{\partial \sigma_{V_{RZ}}^2}{\partial Z} \right), \tag{10}$$

$$\rho K_Z = \frac{\partial(\rho \sigma_{V_Z}^2)}{\partial Z} + \frac{1}{R} \frac{\partial(R \rho \sigma_{V_{RZ}}^2)}{\partial R}. \tag{11}$$

Here, ρ denotes the spatial density of the Galactic component. The circular velocity at the solar radius is adopted as $V_c = 220\,\mathrm{km\,s^{-1}}$, and $\overline{V_\phi}$ is the mean azimuthal velocity of the stellar population characterized by the velocity dispersions σ_{VR}, σ_{V_ϕ}, and σ_{VZ}. The cross term of the velocity-dispersion tensor is defined as $\sigma_{V_{RZ}}^2 = V_R \bar{V}_Z - \bar{V}_R \bar{V}_Z$, while K_Z represents the vertical component of the Galactic gravitational acceleration.

3.5.1. Radial Scale Lengths

We adopt an exponential radial density profile of the form $\rho(R) \propto \exp(-R/h_R)$, and assume that the radial velocity dispersion follows the same functional dependence as the density distribution (e.g., J. Binney & S. Tremaine 2008; J. Bovy & H.-W. Rix 2013). With this assumption, the radial velocity dispersion can be written as $\sigma_{V_R}^2 \propto \exp(-R/h_R)$. Furthermore, we neglect the vertical gradient of the cross term, i.e., $\partial \sigma_{V_{R,Z}}^2 / \partial Z \approx 0$, which is valid for a locally plane-parallel potential corresponding to an infinite constant surface density sheet (G. Gilmore et al. 1989). In this limit, the principal axes of the velocity ellipsoid are aligned with the cylindrical coordinate system, and Equation (10) reduces to

$$\frac{\sigma_{V_\phi}^2}{\sigma_{V_R}^2} - 1 + \frac{2R}{h_R} - \frac{v_c^2 - \bar{v_\phi}^2}{\sigma_{V_R}^2} = 0. \tag{12}$$

Alternatively, if the Galactic potential is dominated by a centrally concentrated mass distribution, the local velocity ellipsoid is expected to be oriented toward the Galactic center (G. Gilmore et al. 1989; J. Binney & S. Tremaine 2008), where the cross-term contribution becomes

$$\frac{r}{\sigma_{V_R}^2} \frac{\partial \sigma_{V_{R,Z}}^2}{\partial Z} \approx 1 - \frac{\sigma_{V_Z}^2}{\sigma_{V_R}^2}. \tag{13}$$

Substituting this approximation into Equation (10) yields

$$\frac{\sigma_{V_\phi}^2}{\sigma_{V_R}^2} - 2 + \frac{2R}{h_R} - \frac{v_c^2 - \bar{v_\phi}^2}{\sigma_{V_R}^2} + \frac{\sigma_{V_Z}^2}{\sigma_{V_R}^2} = 0. \tag{14}$$

All terms appearing in Equations (12) and (14) are directly constrained by the observational data, leaving the radial scale length h_R as the only free parameter of the disk model.

3.5.2. Vertical Scale Heights

Following G. Kordopatis et al. (2011), we neglect the final term in Equation (11), $(1/R)(\partial(R\rho\sigma_{V_{RZ}}^2)/\partial R)$, which represents the radial variation of the cross term of the velocity-dispersion tensor. This approximation is adopted because our sample lies in the solar neighborhood, far from the Galactic center, where this contribution is expected to be small. We further assume that the vertical density profile of the disk component follows an exponential form, $\rho(Z) \propto \exp(-Z/h_Z)$. Under these assumptions, Equation (11) can be rearranged into a more compact form as

$$\frac{\partial \ln \sigma_{V_Z}^2}{\partial Z} + \frac{K_Z}{\sigma_{V_Z}^2} - \frac{1}{h_Z} = 0, \tag{15}$$

which directly relates the vertical gradient of the velocity dispersion to the local gravitational force and the vertical scale height of the Galactic disk.

4. Results

4.1. Spatial Distributions

Figure 1 presents the Aitoff projections of the positions of our sample of WDs in both equatorial and Galactic coordinate systems. The equatorial distribution reflects the observational footprint of the SDSS, which was conducted primarily from the Apache Point Observatory in the Northern Hemisphere. Not surprisingly, ≈91% of the WDs in our sample are located in the northern celestial hemisphere. The distribution becomes slightly more balanced in Galactic coordinates, with approximately 81% of the objects located at positive Galactic latitudes. Although the sample is subject to the selection effects imposed by the SDSS survey geometry, WDs are represented on both sides of the Galactic plane. Furthermore, the SDSS observing strategy preferentially targeted regions with Galactic latitudes of $|b| > 20°$.

Figure 2 shows the distance distribution of our sample based on C. A. L. Bailer-Jones et al. (2021) estimates. Since SDSS spectroscopy is a magnitude-limited survey, we find a skewed distribution characterized by a concentration of nearby objects and a progressively decreasing number of sources at larger distances. The mean, median, and mode of the distribution are 252, 214, and 125 pc, respectively.

Figure 3 shows the distribution of our sample in the heliocentric Galactic Cartesian coordinates (X, Y, Z). Symbols are color coded according to their relative distance uncertainties (d_{err}/d). Our WD sample is roughly symmetrically distributed around the Sun in the Galactocentric X- and Y-coordinates, where the median positions of the sample are found to be at $X = -35$ pc, $Y = 26$ pc, and $Z = 125$ pc. The positive median Z-value indicates that the sample is distributed preferentially above the Galactic plane. This asymmetry is not expected to reflect the intrinsic distribution of nearby WDs, but

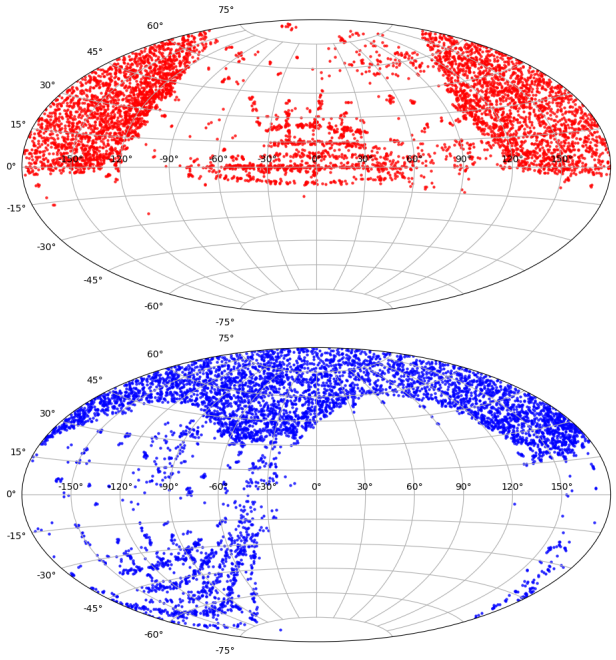


Figure 1. Aitoff projections of our WD sample in the equatorial (α, δ; top panel) and Galactic (l, b; bottom panel) coordinate systems.

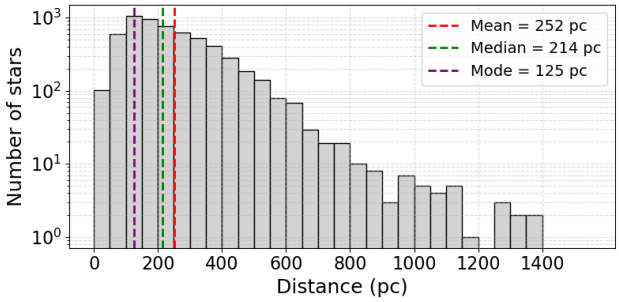


Figure 2. Histogram of the heliocentric distances of the WDs in our sample.

is instead primarily a consequence of the SDSS survey geometry. For comparison, R. Raddi et al. (2022) also found a similar offset in Z of 120 pc using the SDSS DR12 DA WD sample.

4.2. Kinematics

Figure 4 presents the Toomre diagrams constructed for the final sample of 5837 WDs after applying the gravitational redshift, Galactic differential rotation, and LSR corrections. To assess the Galactic population membership of the sample, we consider two widely used kinematic classification schemes. The first adopts fixed total space-velocity thresholds following P. E. Nissen (2004), whereas the second employs the probability-based formalism of T. Bensby et al. (2003, 2005). The two approaches provide complementary views of the kinematic structure of the sample and enable a direct comparison between deterministic and probabilistic population assignments. Using the velocity limits proposed by P. E. Nissen (2004), we classify stars with $S_{\rm LSR} \leqslant 80\,{\rm km\,s^{-1}}$ as thin-disk members, objects with $80 < S_{\rm LSR} \leqslant 180\,{\rm km\,s^{-1}}$ as thick-disk stars, and those with $S_{\rm LSR} > 180\,{\rm km\,s^{-1}}$ as halo candidates. According to these criteria, 5304 (90.9%) WDs belong to the thin disk, 516 (8.8%) to the thick disk, and only

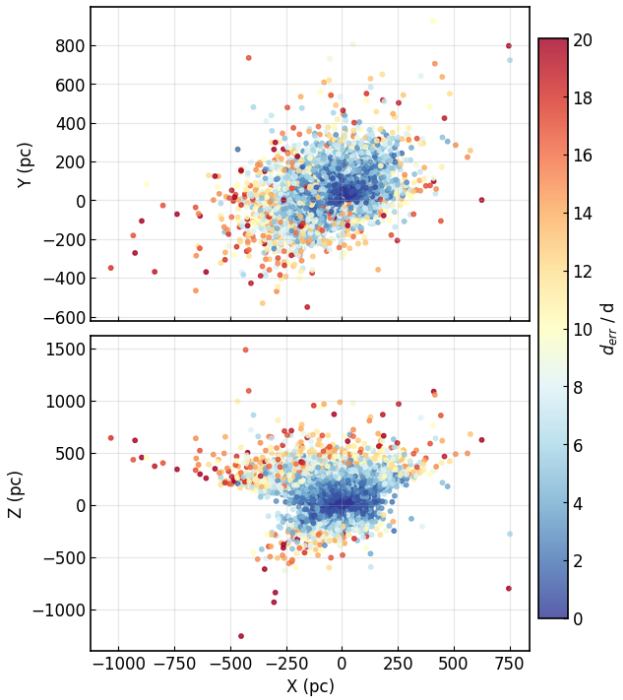


Figure 3. Distribution of the WDs in the heliocentric Galactic Cartesian $X-Y$ (top) and $X-Z$ (bottom) planes. The color scale indicates the relative distance uncertainty.

17 (0.3%) satisfy the halo criterion. The resulting Toomre diagram exhibits the expected kinematic sequence, with thin-disk stars concentrated near the origin and progressively higher-velocity populations occupying the outer regions of the diagram.

The probabilistic classification method of T. Bensby et al. (2003, 2005) accounts for the overlap between the velocity distributions of different Galactic populations. Based on the TD/D probability ratio, we classify 4840 WDs as high-probability thin-disk members ($TD/D \leqslant 0.1$), 628 as low-probability thin-disk members ($0.1 < TD/D \leqslant 1$), and 167 as transition objects between the thin and thick disks ($1 < TD/D \leqslant 10$). For the 202 WDs with $TD/D > 10$, we use the TD/H ratio to distinguish thick-disk from halo members. Of these, 186 WDs with $TD/H > 1$ are assigned to the thick disk, while 16 with $TD/H \leqslant 1$ are classified as halo members. We adopt the classification scheme of T. Bensby et al. (2003, 2005) throughout the remainder of this study. The high- and low-probability thin-disk categories are combined, yielding a final thin-disk sample of 5468 WDs with $TD/D \leqslant 1$. The 167 objects with $1 < TD/D \leqslant 10$ are treated as kinematic transition objects and are not included in any of the three final population samples. Our classified sample therefore consists of 5468 thin-disk, 186 thick-disk, and 16 halo WDs. Among the 5670 WDs assigned to a specific Galactic population, these numbers correspond to observed fractions of 96.4%, 3.3%, and 0.3%, respectively. Thus, the solar-neighborhood WD sample examined here is overwhelmingly dominated by the thin-disk population. A similarly small halo contribution ($\sim$1%) was recently reported by A. Swan et al. (2026) for the DESI DR1 WD sample. Although their probabilistic disk–halo decomposition differs from the population criteria adopted here, both analyses consistently indicate that disk stars overwhelmingly

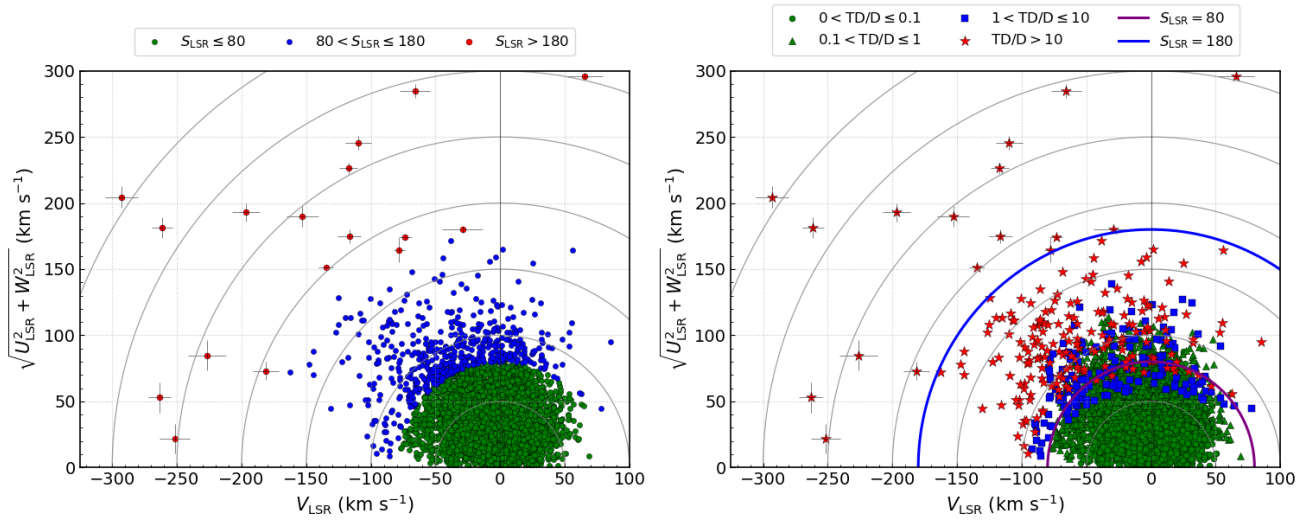


Figure 4. Toomre diagrams for our WD sample. The two panels show the Galactic population classification based on S_{tot} (P. E. Nissen 2004; left) and the kinematic criteria of T. Bensby et al. (2003, 2005; right). The gray curves represent iso-total-velocity contours, while the blue and purple curves denote the velocity boundaries adopted to distinguish the thick- and thin-disk populations, respectively.

dominate the local WD population, with only a minor contribution from the halo.

4.3. Galactic Orbital Properties

The orbital integrations described in Section 3.3 provide the Galactic orbital parameters (R_{peri}, R_{apo}, Z_{max}, e, R_g, and P_{orb}) for all 5837 WDs in the final kinematic sample. The equatorial and Galactic coordinates, velocity components, orbital parameters, total ages, and progenitor masses for a representative subset of the studied WDs are listed in Appendix (Table A1), while the complete catalog is available in the online supplementary material.

The orbital parameter distributions reveal that the sample spans a broad range of dynamical properties. Most WDs follow nearly circular orbits confined to the Galactic disk, as indicated by their low eccentricities and small values of Z_{max}. Nevertheless, a small fraction of the sample reaches several kpc above the Galactic plane, with a few objects attaining $Z_{max} \sim 10$ kpc. While the eccentricity distribution is strongly peaked toward low values, a limited number of stars exhibit highly eccentric orbits. These objects are consistent with dynamically hotter populations associated with the thick disk and halo.

Figure 5 shows the distribution of the sample in the Z_{max} versus e plane, where the kinematic populations identified using the T. Bensby et al. (2003, 2005) criteria are indicated. As expected, thin-disk WDs are concentrated at low eccentricities and short vertical distances, whereas thick-disk and halo candidates occupy progressively larger regions of the diagram. However, a small number of stars exhibit relatively large eccentricities despite remaining confined to $Z_{max} < 1$ kpc. These objects possess dynamically hot radial orbits while remaining close to the Galactic plane, suggesting that radial migration and orbital blurring have played an important role in shaping their present-day orbital properties.

4.4. Velocity Dispersions and Population Properties

Table 2 presents the Galactic velocity components and their dispersions, total stellar ages, progenitor masses, and orbital

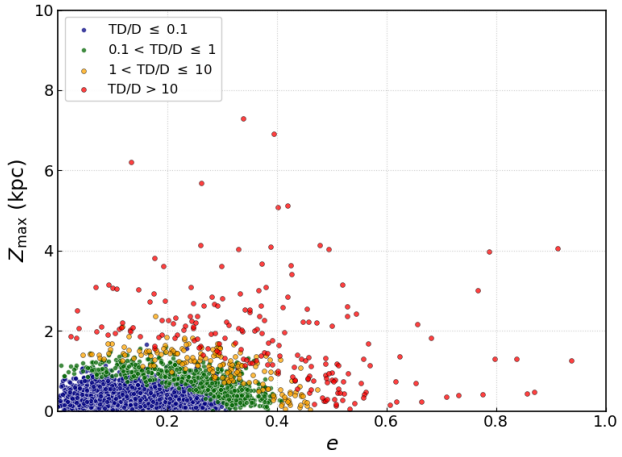


Figure 5. Z_{max} vs. eccentricity for our WD sample. Each object is color coded according to its population membership based on the kinematic criteria of T. Bensby et al. (2003, 2005).

eccentricities for the different subsamples. For the entire sample, the mean velocity components relative to the LSR are $\langle U_{LSR} \rangle = -0.4 \pm 4.3$ km s^{-1}, $\langle V_{LSR} \rangle = -7.5 \pm 3.8$ km s^{-1}, and $\langle W_{LSR} \rangle = -1.5 \pm 6.3$ km s^{-1}. The corresponding velocity dispersions are $\sigma_U = 38.1 \pm 0.4$ km s^{-1}, $\sigma_V = 27.7 \pm 0.3$ km s^{-1}, and $\sigma_W = 24.4 \pm 0.2$ km s^{-1}, yielding a total velocity dispersion of $\sigma_{tot} = 53.0 \pm 0.5$ km s^{-1}. The measured velocity dispersions define an anisotropic velocity ellipsoid typical of the Galactic disk. Such a distribution is consistent with the secular dynamical evolution of the Galactic disk, in which stellar random motions are amplified more efficiently in the radial direction than perpendicular to the disk. For the complete sample, the median total age, progenitor mass, and Galactic orbital eccentricity are 4.4 Gyr, 1.66 $M_\odot$, and 0.16, respectively. The median age and low orbital eccentricity are consistent with the predominance of thin-disk WDs in the sample, while the inferred progenitor mass corresponds to an intermediate-mass main-sequence star.

When the sample is divided according to the total space velocity (P. E. Nissen 2004), the total velocity dispersion increases steadily from $\sigma_{tot} = 43.3 \pm 0.4$ km s^{-1} for stars with $S_{LSR} \leqslant 80$ km s^{-1} to 201.0 ± 35.5 km s^{-1} for the highest-

Table 2

Mean Space-velocity Components and Their Dispersions, Total Ages, Mean Progenitor Masses, and Mean Galactic Orbital Eccentricities of the White Dwarfs Classified into Galactic Populations According to Four Different Criteria

Criterion	N	$U_{\rm LSR}$	$V_{\rm LSR}$	$W_{\rm LSR}$	σ_U (km s^{-1})	σ_V	σ_W	$\sigma_{\rm tot}$	$\langle t_{\rm tot}\rangle$ (Gyr)	$\langle M\rangle$ ($M_\odot$)	$\langle e\rangle$
Full sample	5837	-0.44 ± 4.30	-7.48 ± 3.76	-1.47 ± 6.26	38.10 ± 0.35	27.66 ± 0.26	24.37 ± 0.23	53.01 ± 0.49	4.42	1.66	0.16
$S_{\rm tot} \leqslant 80$ km s^{-1}	5304	0.14 ± 4.18	-4.21 ± 3.65	-1.67 ± 6.18	31.39 ± 0.30	22.31 ± 0.22	19.88 ± 0.19	43.34 ± 0.42	4.36	1.67	0.14
$80 < S_{\rm tot} \leqslant 180$ km s^{-1}	516	-5.46 ± 5.49	-36.50 ± 4.76	2.01 ± 7.07	75.25 ± 2.34	40.81 ± 1.27	45.96 ± 1.43	97.16 ± 3.03	5.10	1.56	0.34
$S_{\rm tot} > 180$ km s^{-1}	17	-29.74 ± 5.69	-146.19 ± 6.51	-44.41 ± 7.68	131.84 ± 23.31	93.29 ± 16.49	119.62 ± 21.15	200.98 ± 35.53	5.01	1.45	0.66
$TD/D \leqslant 0.1$	4840	0.82 ± 4.19	-3.35 ± 3.59	-1.25 ± 6.09	32.33 ± 0.33	19.64 ± 0.20	16.03 ± 0.16	41.08 ± 0.42	4.33	1.67	0.13
$0.1 < TD/D \leqslant 1$	628	-4.27 ± 4.75	-16.50 ± 4.34	-4.78 ± 6.89	51.37 ± 1.45	36.59 ± 1.03	33.59 ± 0.95	71.46 ± 2.02	4.93	1.54	0.25
$1 < TD/D < 10$	167	-10.93 ± 4.72	-27.94 ± 4.60	1.27 ± 7.13	56.49 ± 3.10	40.23 ± 2.21	46.31 ± 2.54	83.39 ± 4.58	4.92	1.63	0.29
$TD/D > 10$	202	-9.95 ± 5.20	-61.47 ± 5.31	1.48 ± 7.67	76.17 ± 3.80	58.65 ± 2.93	75.31 ± 3.76	122.12 ± 6.09	4.78	1.67	0.39
Thin disk	5468	0.23 ± 4.26	-4.86 ± 3.68	-1.66 ± 6.18	35.08 ± 0.34	22.64 ± 0.22	18.93 ± 0.18	45.84 ± 0.44	4.40	1.66	0.15
Thick disk	186	-10.71 ± 5.20	-54.33 ± 5.16	3.56 ± 7.59	70.72 ± 3.68	46.63 ± 2.42	67.02 ± 3.48	108.02 ± 5.62	4.71	1.69	0.38
Halo	16	-1.08 ± 5.24	-144.52 ± 7.08	22.80 ± 8.63	122.53 ± 22.37	103.29 ± 18.86	136.90 ± 24.99	210.77 ± 38.48	4.41	1.40	0.65
$Z_{\rm max} \leqslant 1$	5408	-0.19 ± 4.26	-6.74 ± 3.72	-1.61 ± 6.14	36.26 ± 0.35	25.31 ± 0.24	17.72 ± 0.17	47.64 ± 0.46	4.38	1.66	0.15
$1 < Z_{\rm max} \leqslant 4$	412	-3.78 ± 4.88	-15.37 ± 4.29	1.16 ± 7.77	54.36 ± 1.90	43.03 ± 1.50	57.67 ± 2.01	90.18 ± 3.15	5.05	1.59	0.23
$Z_{\rm max} > 4$	17	1.94 ± 3.62	-53.49 ± 5.07	-19.05 ± 8.43	90.97 ± 16.08	100.41 ± 17.75	151.39 ± 26.76	203.17 ± 35.92	3.72	2.17	0.44

velocity subsample ($S_{\rm LSR} > 180\,{\rm km\ s^{-1}}$). This increase is accompanied by progressively larger dispersions in all three velocity components and by a pronounced decrease in the mean rotational velocity, reaching $\langle V_{\rm LSR}\rangle = -146.2 \pm 6.5\,{\rm km\ s^{-1}}$ for the fastest stars, indicative of a substantial rotational lag with respect to the Galactic disk. At the same time, the median total age of the WDs increases from 4.4 to 5.0 Gyr, while the median progenitor mass decreases from 1.67 to 1.45 $M_{\odot}$, and the median Galactic orbital eccentricity rises from 0.14 to 0.66. These systematic trends indicate a gradual transition from a sample dominated by dynamically cold thin-disk WDs to a population with larger contributions from the thick disk and the halo. The increasing Galactic orbital eccentricities reflect the transition from nearly circular disk orbits to the more elliptical orbits characteristic of dynamically hotter Galactic populations.

A similar kinematic progression is recovered when the WDs are classified as thin-disk, thick-disk, and halo members using the population probabilities of T. Bensby et al. (2003, 2005). Objects with $1 < TD/D \leqslant 10$ were classified as transition objects and excluded from the final population samples. The thin-disk population, comprising 5468 WDs, has mean space velocities of $(U_{\rm LSR}, V_{\rm LSR}, W_{\rm LSR}) = (0.2, -4.9, -1.7)\,{\rm km\ s^{-1}}$ and exhibits the smallest velocity dispersions, with $(\sigma_U, \sigma_V, \sigma_W) = (35.1, 22.6, 18.9)\,{\rm km\ s^{-1}}$ and $\sigma_{\rm tot} = 45.8 \pm 0.4\,{\rm km\ s^{-1}}$. For the 186 thick-disk WDs, the corresponding mean space-velocity components are $(U_{\rm LSR}, V_{\rm LSR}, W_{\rm LSR}) = (-10.7, -54.3, 3.6)\,{\rm km\ s^{-1}}$, while the space-velocity component dispersions increase to $(\sigma_U, \sigma_V, \sigma_W) = (70.7, 46.6, 67.0)\,{\rm km\ s^{-1}}$, yielding $\sigma_{\rm tot} = 108.0 \pm 5.6\,{\rm km\ s^{-1}}$. The 16 halo WDs show the largest rotational lag, with $(U_{\rm LSR}, V_{\rm LSR}, W_{\rm LSR}) = (-1.1, -144.5, 22.8)\,{\rm km\ s^{-1}}$, and the broadest velocity distribution, characterized by $(\sigma_U, \sigma_V, \sigma_W) = (122.5, 103.3, 136.9)\,{\rm km\ s^{-1}}$ and $\sigma_{\rm tot} = 210.8 \pm 38.5\,{\rm km\ s^{-1}}$. Thus, the increasingly negative mean $V_{\rm LSR}$ and the systematic growth of both the component and total velocity dispersions from the thin disk to the halo reflect progressively hotter stellar kinematics and a larger rotational lag. This trend is particularly pronounced in σ_W, indicating progressively stronger vertical dynamical heating from the thin disk to the halo. The orbital eccentricities show a consistent progression, with their mean value increasing from 0.15 for the thin disk to 0.38 for the thick disk and 0.65 for the halo.

A consistent picture is also obtained when the WDs are classified according to their maximum distance from the Galactic plane ($Z_{\rm max}$). Following the adopted criteria, stars with $Z_{\rm max} \leqslant 1\,{\rm kpc}$, $1 < Z_{\rm max} \leqslant 4\,{\rm kpc}$, and $Z_{\rm max} > 4\,{\rm kpc}$ are assigned to the thin-disk, thick-disk, and halo populations, respectively. The total velocity dispersion increases systematically from $\sigma_{\rm tot} = 47.6\,{\rm km\ s^{-1}}$ for the thin-disk population to $\sigma_{\rm tot} = 203.2\,{\rm km\ s^{-1}}$ for the halo population. In contrast, the median total ages do not exhibit a monotonic variation across the three Galactic populations, even though the Galactic orbital eccentricities increase steadily from 0.15 for the thin-disk population to 0.44 for the halo population. Overall, the kinematic trends obtained from the $Z_{\rm max}$-based subsamples are consistent with those inferred from the velocity- and probability-based classifications. Both the velocity dispersions and orbital eccentricities increase systematically from the thin disk to the halo, whereas neither the median total age nor the progenitor mass exhibits a similarly robust correlation with Galactic population. The absence of a clear age or progenitor-mass sequence should, however, be interpreted with caution, since the halo subsample contains only a limited number of objects, reducing the statistical significance of any evolutionary trends involving this population.

4.5. Age–Velocity Dispersion Relations

To investigate the age dependence of WD kinematics, we analyzed the AVR using the subset of 4829 WDs for which total stellar ages could be determined with the `wdwarfdate` package (R. Kiman et al. 2022). To assess the effect of population contamination, the analysis was carried out on three samples: (1) the complete sample with available total stellar ages ($N = 4829$), (2) a kinematically selected thin-disk sample ($N = 4578$) satisfying $TD/D \leqslant 1$ (T. Bensby et al. 2003, 2005), and (3) a sample ($N = 4537$) restricted to $Z_{\rm max} \leqslant 1$ kpc. In each sample, stars were grouped into 1 Gyr age bins. For each age bin, the velocity dispersions σ_U, σ_V, and σ_W were calculated as the sample standard deviations of the corresponding $U_{\rm LSR}$, $V_{\rm LSR}$, and $W_{\rm LSR}$ velocity components, while $\sigma_{\rm tot}$ was calculated from $S_{\rm LSR}$. The median age of each bin was adopted as the representative age to minimize the influence of outliers. The uncertainty in each velocity dispersion was estimated from the standard error of the sample standard deviation, $\epsilon_{\sigma_i} = \sigma_i/\sqrt{2(N-1)}$, where N is the number of WDs in the corresponding age bin (I. Joncour et al. 2017). The AVR relation $\sigma_i = A \times t^B$ was fitted to the binned velocity dispersions using an unweighted fit, and the goodness of each fit was quantified by the coefficient of determination (R^2). Individual WD total ages can have substantial and asymmetric uncertainties, particularly because uncertainties in the WD parameters propagate into the inferred progenitor masses and pre-WD evolutionary lifetimes. In some cases, the upper uncertainty limits may extend beyond the age of the Galaxy. We therefore interpret the AVR on a statistical, population-wide basis rather than assigning significance to the age of any individual WD. The use of 1 Gyr age bins and the median age within each bin reduces the sensitivity to individual extreme age estimates; nevertheless, age uncertainties may broaden the distributions and contribute to the observed scatter in the AVR.

Figure 6 and Table 3 show the AVR for these three subsamples, where a clear increase in velocity dispersion with increasing total age is observed. For the complete sample, the total space-velocity dispersion increases from $\sigma_{\rm tot} = 39.2\,{\rm km\ s^{-1}}$ for the youngest population (<1 Gyr) to $57.6\,{\rm km\ s^{-1}}$ for stars older than 8 Gyr. A similar monotonic increase is calculated for the individual space-velocity components, with the radial component exhibiting the strongest evolution, increasing from $\sigma_U = 26.5$ to $42.0\,{\rm km\ s^{-1}}$. The azimuthal component grows from $\sigma_V = 19.2$ to $29.4\,{\rm km\ s^{-1}}$, whereas the vertical space-velocity component increases more gradually, from $\sigma_W = 21.6$ to $26.2\,{\rm km\ s^{-1}}$. These trends indicate that older WDs have experienced more prolonged dynamical heating through cumulative gravitational perturbations within the Galactic disk.

To quantify the AVR, each velocity component was fitted with a power-law relation of the form $\sigma_{\rm i} = A \times t^B$, where t is the total stellar age in Gyr. For the complete sample, the best-fitting exponents are $B = 0.155 \pm 0.015$, 0.167 ± 0.033, 0.058 ± 0.029, and 0.137 ± 0.019 for the σ_U, σ_V, σ_W, and $\sigma_{\rm tot}$, respectively (Table 4). The relatively large exponents found for the radial and azimuthal components demonstrate that in-plane stellar motions continue to be dynamically heated

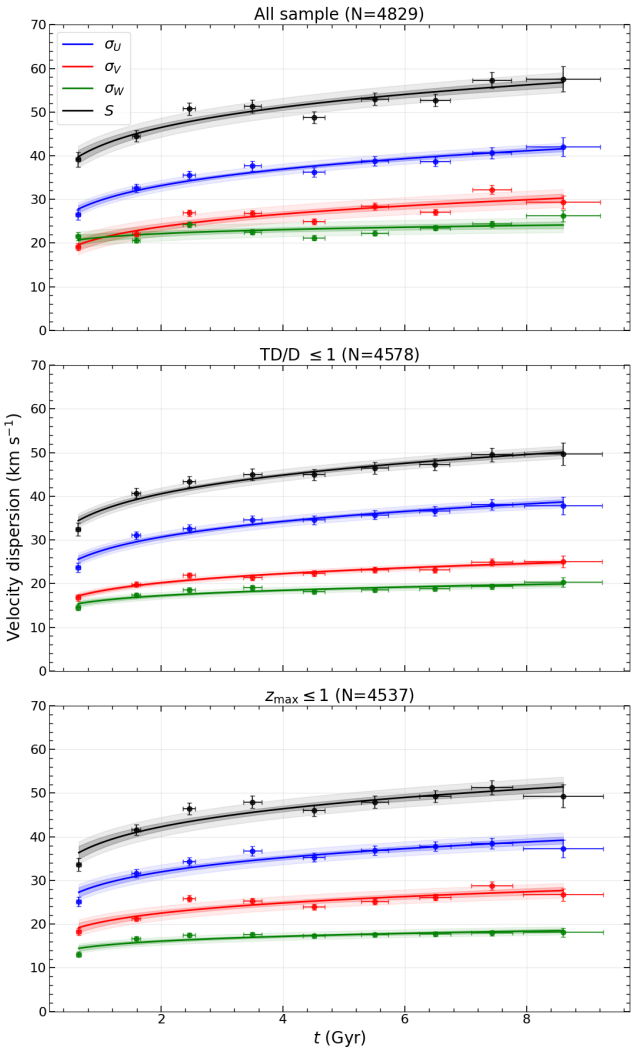


Figure 6. Velocity dispersion vs. age for the entire WD sample (top), those classified as thin-disk members ($TD/D \leqslant 1$) according to the kinematic criteria of T. Bensby et al. (2003, 2005; middle), and those with $Z_{max} \leqslant 1$ kpc (bottom).

throughout the lifetime of the Galactic disk. In contrast, the substantially smaller exponent obtained for the vertical component suggests that vertical heating proceeds more slowly than radial heating, consistent with expectations for secular disk evolution.

The same overall behavior is recovered in both thin-disk subsamples, although with systematically lower velocity dispersions owing to the reduced contribution from thick-disk and halo stars. In the kinematically selected thin-disk sample ($TD/D \leqslant 1$), the total space-velocity dispersion increases from $\sigma_{tot} = 32.4$ to 49.7 km s^{-1}, while the orbital thin-disk sample ($Z_{max} \leqslant 1$ kpc) exhibits a comparable increase from $\sigma_{tot} = 33.7$ to 49.3 km s^{-1}. The vertical space-velocity dispersion remains consistently lower in the orbital sample, reflecting the explicit exclusion of stars reaching large distances from the Galactic plane. The power-law indices derived for both thin-disk samples ($B \approx 0.10$–0.16) closely match those obtained for the full sample, confirming that the observed AVR is an intrinsic property of the thin-disk WD population rather than a consequence of contamination by older Galactic components.

The observed increase in velocity dispersion with total age provides strong evidence that WDs retain the dynamical signatures of the secular heating history of the Galactic disk (e.g., N. Rowell & M. Kilic 2019; R. Raddi et al. 2022). The derived power-law exponents ($B \approx 0.06$–0.17) are comparable to those reported for other Galactic stellar populations, indicating that WDs follow the same long-term dynamical evolution despite spanning a wide range of progenitor masses and evolutionary histories (e.g., J. Holmberg et al. 2009; Y.-S. Ting & H.-W. Rix 2019). The stronger age dependence of the radial velocity dispersion further supports the interpretation that scattering by giant molecular clouds, spiral arms, and the Galactic bar has played a dominant role in shaping the kinematic evolution of the local WD population (e.g., I. Minchev & B. Famaey 2010; R. J. J. Grand et al. 2016).

4.6. Radial Migration and Orbital Blurring across Galactic Populations

We reconstruct the birth radii (R_b) of each WD by integrating their Galactic orbits backward over their total stellar ages following the methodology of F. Akbaba et al. (2024). Because metallicity-based estimates are unavailable, we take each star's Galactocentric radius at that lookback time as an estimate of its birth radius. This assumes that the adopted Galactic potential approximates the star's past orbit; the integration cannot independently recover changes in angular momentum caused by past interactions. We propagate uncertainties in the astrometric parameters, distances, proper motions, and radial velocities through the orbital integrations to estimate the uncertainties in R_b. We then compare R_b with the present guiding radius (R_g) and Galactocentric radius (R_{gc}). Interpretations of the resulting displacements and migration directions depend on the adopted birth-radius estimate. For comparison, we overplot the age-dependent radial-migration relations of N. Frankel et al. (2018, 2020) as presented in Figure 9 of M. Netopil et al. (2022). These curves are used only as a reference; no additional transformations of the dynamical quantities reported by N. Frankel et al. (2018, 2020) were applied. WDs lying below or above these curves exhibit radial displacements that are smaller or larger, respectively, than the corresponding reference values at a given age. However, these differences should not be interpreted directly as evidence for weaker or stronger dynamical interactions, because the inferred displacements also depend on individual orbital histories, birth radii, age uncertainties, and the assumptions underlying the migration models.

Figure 7 presents $|R_g - R_b|$ and $|R_{gc} - R_b|$ for the thin-disk, thick-disk, and halo WDs in separate panels. For this analysis, we separate the populations using the S_{LSR} values, following the kinematic criteria of P. E. Nissen (2004). This velocity-based assignment is distinct from the probability-based classification used elsewhere in the paper. The difference $|R_g - R_b|$ compares the present R_g with the inferred R_b and thus serves as a proxy for radial migration associated with changes in angular momentum. By contrast, $|R_{gc} - R_b|$ uses the present-day R_{gc}: it includes both the displacement of the guiding radius and the star's current epicyclic excursion about that radius. The two quantities therefore describe related, but nonadditive, aspects of radial redistribution.

We show their age dependence using the median displacement in 0.5 Gyr bins. The error bars show the standard deviation within each bin, while the red lines mark the mean

Table 3
Total Number of White Dwarfs, Mean Ages, and Space-velocity Dispersions for Different Total Stellar Age Bins

Sample	Age range (Gyr)	N	$\langle t \rangle$ (Gyr)	σ_U	σ_V (km s^{-1})	σ_W	$\sigma_{\rm tot}$
Full sample ($N = 4829$)	0–1	271	0.64 ± 0.04	26.48 ± 1.14	19.16 ± 0.82	21.59 ± 0.93	39.17 ± 1.68
	1–2	614	1.59 ± 0.06	32.63 ± 0.93	22.11 ± 0.63	20.65 ± 0.59	44.50 ± 1.27
	2–3	656	2.46 ± 0.10	35.58 ± 0.98	26.91 ± 0.74	24.21 ± 0.67	50.76 ± 1.40
	3–4	601	3.50 ± 0.14	37.65 ± 1.09	26.73 ± 0.77	22.53 ± 0.65	51.38 ± 1.48
	4–5	627	4.51 ± 0.18	36.22 ± 1.02	24.94 ± 0.70	21.16 ± 0.60	48.80 ± 1.37
	5–6	643	5.51 ± 0.22	38.79 ± 1.08	28.44 ± 0.79	22.26 ± 0.62	53.00 ± 1.47
	6–7	696	6.50 ± 0.25	38.63 ± 1.04	27.06 ± 0.73	23.49 ± 0.63	52.69 ± 1.42
	7–8	524	7.43 ± 0.32	40.62 ± 1.26	32.25 ± 1.00	24.35 ± 0.75	57.30 ± 1.77
	>8	197	8.60 ± 0.61	42.01 ± 2.12	29.40 ± 1.48	26.20 ± 1.32	57.58 ± 2.90
$TD/D \leqslant 1$ ($N = 4578$)	0–1	258	0.64 ± 0.04	23.68 ± 1.04	16.74 ± 0.74	14.51 ± 0.64	32.43 ± 1.43
	1–2	595	1.59 ± 0.07	31.02 ± 0.90	19.82 ± 0.58	17.34 ± 0.50	40.69 ± 1.18
	2–3	624	2.46 ± 0.10	32.55 ± 0.92	21.86 ± 0.62	18.53 ± 0.52	43.37 ± 1.23
	3–4	569	3.50 ± 0.15	34.57 ± 1.03	21.41 ± 0.64	19.13 ± 0.57	44.94 ± 1.34
	4–5	601	4.51 ± 0.18	34.53 ± 1.00	22.32 ± 0.64	18.14 ± 0.52	44.94 ± 1.30
	5–6	609	5.51 ± 0.22	35.69 ± 1.02	23.13 ± 0.66	18.55 ± 0.53	46.40 ± 1.33
	6–7	650	6.49 ± 0.25	36.61 ± 1.02	23.13 ± 0.64	18.87 ± 0.52	47.24 ± 1.31
	7–8	491	7.43 ± 0.34	38.15 ± 1.22	24.90 ± 0.80	19.31 ± 0.62	49.48 ± 1.59
	>8	181	8.60 ± 0.64	37.80 ± 1.99	25.06 ± 1.32	20.27 ± 1.07	49.68 ± 2.62
$Z_{\rm max} \leqslant 1$ kpc ($N = 4537$)	0–1	255	0.65 ± 0.04	25.11 ± 1.11	18.23 ± 0.81	13.05 ± 0.58	33.66 ± 1.49
	1–2	593	1.59 ± 0.07	31.65 ± 0.92	21.28 ± 0.62	16.69 ± 0.49	41.63 ± 1.21
	2–3	623	2.46 ± 0.10	34.34 ± 0.97	25.83 ± 0.73	17.52 ± 0.50	46.40 ± 1.31
	3–4	564	3.50 ± 0.15	36.74 ± 1.09	25.24 ± 0.75	17.58 ± 0.52	47.92 ± 1.42
	4–5	599	4.51 ± 0.18	35.26 ± 1.02	23.91 ± 0.69	17.27 ± 0.50	45.97 ± 1.33
	5–6	606	5.51 ± 0.22	36.91 ± 1.06	25.13 ± 0.72	17.54 ± 0.50	47.97 ± 1.38
	6–7	647	6.50 ± 0.26	37.79 ± 1.05	26.10 ± 0.73	17.73 ± 0.49	49.23 ± 1.37
	7–8	479	7.43 ± 0.34	38.47 ± 1.24	28.74 ± 0.93	17.96 ± 0.58	51.27 ± 1.65
	>8	171	8.60 ± 0.66	37.33 ± 2.02	26.70 ± 1.45	18.07 ± 0.98	49.32 ± 2.67

Table 4
Best-fit Parameters of the Age–Velocity Dispersion Relation, $\sigma = A \times t^B$, for the Three White Dwarf Samples

Sample	σ (km s^{-1})	A	B	R^2
Full sample	σ_U	29.76 ± 0.73	0.155 ± 0.015	0.945
	σ_V	21.12 ± 1.13	0.167 ± 0.033	0.808
($N = 4829$)	σ_W	21.28 ± 0.95	0.058 ± 0.029	0.373
	$\sigma_{\rm tot}$	42.25 ± 1.24	0.137 ± 0.019	0.898
$TD/D \leqslant 1$	σ_U	27.44 ± 0.70	0.160 ± 0.016	0.944
	σ_V	18.28 ± 0.38	0.143 ± 0.013	0.950
($N = 4578$)	σ_W	16.09 ± 0.46	0.099 ± 0.018	0.824
	$\sigma_{\rm tot}$	36.69 ± 0.79	0.145 ± 0.013	0.950
$Z_{\rm max} \leqslant 1$ kpc	σ_U	28.99 ± 0.94	0.140 ± 0.020	0.887
	σ_V	20.40 ± 0.92	0.142 ± 0.028	0.803
($N = 4537$)	σ_W	15.06 ± 0.52	0.095 ± 0.022	0.748
	$\sigma_{\rm tot}$	38.53 ± 1.26	0.134 ± 0.021	0.875

Note. The fitted coefficients A and B and the corresponding correlation coefficients (R^2) are listed.

displacement of each disk subsample. The thin-disk WDs have mean $|R_{\rm g} - R_{\rm b}|$ and $|R_{\rm gc} - R_{\rm b}|$ values of 0.55 ± 0.58 and 0.73 ± 0.83 kpc, respectively. The median $|R_{\rm g} - R_{\rm b}|$ increases modestly from the youngest bins to ages of about 7–8 Gyr, although the sequence is not monotonic. The median $|R_{\rm gc} - R_{\rm b}|$ shows no clear age trend. At ages of a few Gyr and older, most thin-disk WDs fall below the reference relations. The thick-disk WDs show larger mean displacements, 1.82 ± 1.42 kpc in $|R_{\rm g} - R_{\rm b}|$ and 1.57 ± 1.55 kpc in $|R_{\rm gc} - R_{\rm b}|$. Their medians vary substantially with age and do not establish a monotonic trend. Only 11 halo WDs have total stellar ages. Their displacements span a wide range, but the small sample does not support a characteristic migration distance or a reliable age trend.

Comparison of the $R_{\rm g}$ and $R_{\rm gc}$ displacements shows that the characteristic values inferred from the two measures are of comparable magnitude in both disk populations. The displacement relative to $R_{\rm g}$ is therefore substantial compared with that relative to the present-day position, under our adopted estimate of $R_{\rm b}$. However, because $|R_{\rm g} - R_{\rm b}|$ and $|R_{\rm gc} - R_{\rm b}|$ do not constitute a strict additive decomposition of radial migration and orbital blurring, we do not assign separate fractional contributions to these two processes.

We examine the direction of radial migration by comparing the reconstructed birth radius $R_{\rm b}$ with the present-day guiding radius. WDs with $R_{\rm g} - R_{\rm b} > 0$ kpc are classified as outward migrators, whereas those with $R_{\rm g} - R_{\rm b} < 0$ kpc are identified as inward migrators. Figure 8 illustrates the distribution of migration direction as a function of $R_{\rm gc}$, with stellar ages indicated by the color scale. Among the 4829 WDs with reliable total ages, 1933 stars (40%) migrated outward from the inner Galactic disk, while 2896 stars (60%) migrated inward from larger Galactocentric radii. The outward-migrating population exhibits a mean radial displacement of +0.57 kpc and a mean age of 4.3 Gyr, whereas the inward migrators show an average displacement of −1.00 kpc and a mean age of 4.5 Gyr. The nearly identical mean ages of the two groups indicate that the asymmetry is not driven by age.

Although inward migrators outnumber outward migrators in the present sample, this imbalance is not evidence for a globally preferred inward migration pattern. Radial-migration models generally permit migration in both directions. The diffusion model of N. Frankel et al. (2018) can produce an

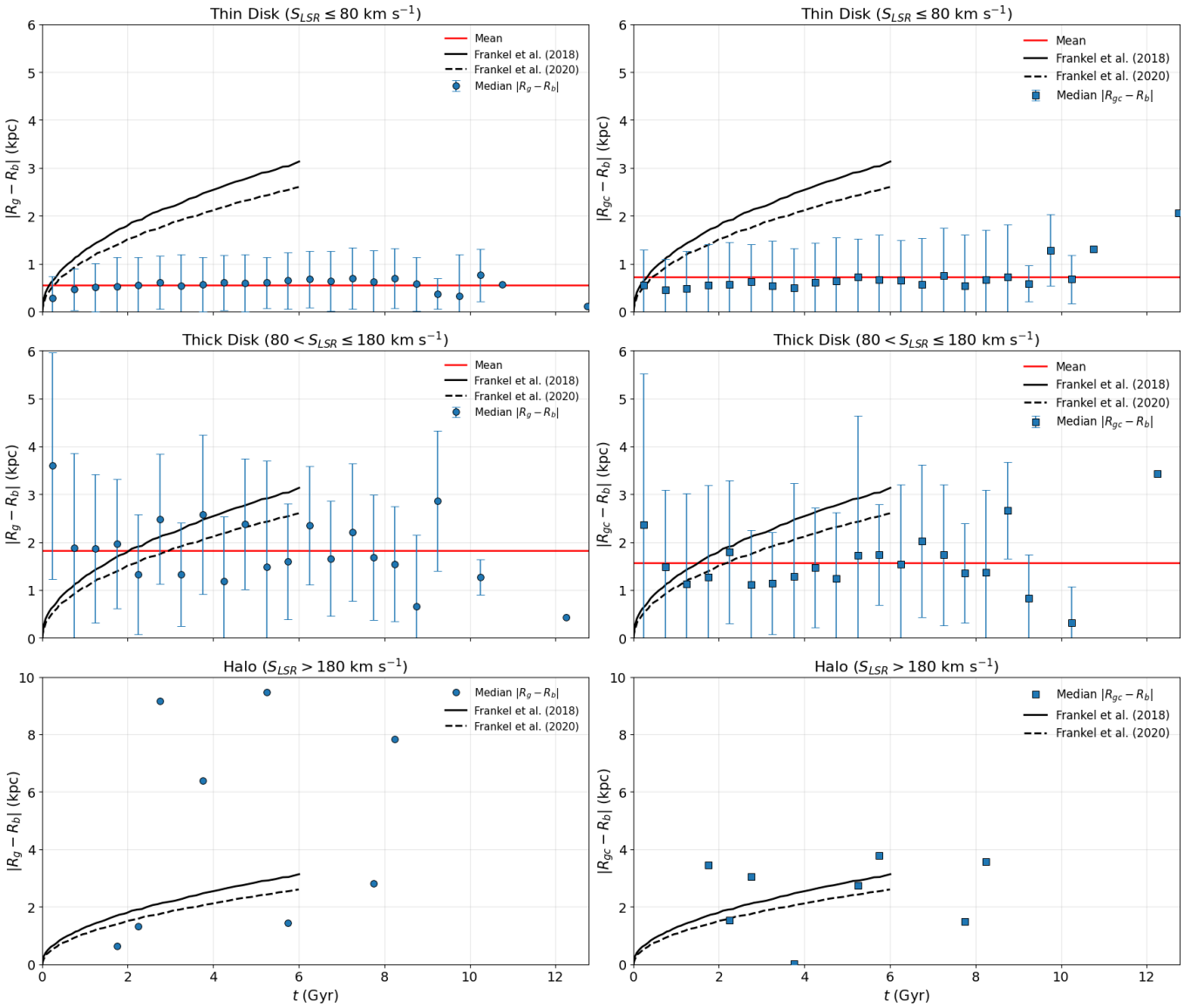


Figure 7. Radial displacement vs. total stellar age for thin-disk (top), thick-disk (middle), and halo (bottom) WDs. The left and right columns show $|R_g - R_b|$ and $|R_{gc} - R_b|$, respectively. The populations are separated at $S_{LSR} = 80$ and 180 km s^{-1}. Blue symbols show the median displacement in 0.5 Gyr age bins; error bars show the standard deviation within each bin. Red horizontal lines mark the mean displacement for each disk subsample. The solid and dashed black curves are the reference relations of N. Frankel et al. (2018, 2020), respectively.

overall outward broadening of the stellar disk, whereas the updated model of N. Frankel et al. (2020) includes a small inward drift term to approximately conserve angular momentum, making inward migration somewhat more probable while retaining substantial migration in both directions. Thus, the relative numbers of inward and outward migrators are model dependent rather than a universal prediction of radial-migration theory. Given the uneven sky coverage of the SDSS observations, our sample does not provide a spatially complete census of the Galactic disk. Approximately 63% of the objects in our sample lie inside the solar circle, whereas 37% are located outside of it, closely matching the relative fractions of inward and outward migrators. Hence, the observed asymmetry in the number of inward and outward migrators is likely due to the observational biases in the SDSS. Future analyses using more spatially complete WD samples will be essential for more stringent constraints on the global migration pattern of the Milky Way disk.

4.7. Disk Scale Height and Scale Length

We use three different subsamples to constrain the radial and vertical scale lengths of the Galactic disk and to investigate how the adopted population affects the inferred Galactic structure. The subsamples are selected based on (i) the present-day vertical distance from the Galactic plane ($|Z| < 800$ pc), (ii) the kinematic population probabilities of T. Bensby et al. (2003, 2005), and (iii) the maximum orbital height above the Galactic plane ($Z_{\rm max}$).

Table 5 presents the Galactocentric cylindrical velocity components and their corresponding velocity dispersions for each subsample. The derived kinematic properties clearly distinguish the thin- and thick-disk populations. The thin-disk subsamples are characterized by mean radial and vertical velocities close to zero together with mean rotational velocities $\langle V_\phi \rangle$ between -207 and -210 km s^{-1}, indicating that these stars participate in the regular rotation of the Galactic disk. In

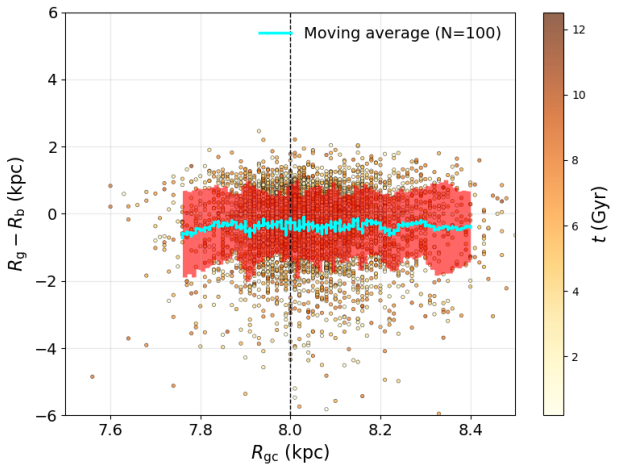


Figure 8. Radial displacement ($|R_g - R_b|$ vs. the present-day Galactocentric radius (R_{gc}) for the WDs in our sample. Each object is color coded according to its total age. The dashed line marks the Galactocentric distance of the Sun, the cyan curve represents the moving average, and the red shaded region shows the 1σ interval.

contrast, the thick-disk sample exhibits a substantially lower rotational velocity, $\langle V_\phi \rangle \approx -165$ km s^{-1}, and larger velocity dispersions, particularly in the vertical direction ($\sigma_{V_Z} = 57.7$ km s^{-1}).

The vertical scale heights were determined using Equation (15), which combines the measured vertical velocity dispersions with their vertical gradients and the corresponding vertical Galactic force (K_Z). The velocity-dispersion gradients were estimated from the variation of σ_{V_Z} with both the present-day vertical distance and the maximum orbital height (Figure 9), while the adopted K_Z values were obtained from the $K_Z(Z)$ relation presented in Figure 14 of K. Kuijken & G. Gilmore (1989). Representative K_Z values were selected according to the vertical ranges adopted for the two disk populations, $0 < |Z| \leqslant 1$ kpc for the thin disk and $1 < |Z| \leqslant 4$ kpc for the thick disk. For the thin disk, we adopted $K_Z = 1.93$ (km s^{-1})^2 pc^{-1} for the vertical distance interval $|Z| \leqslant 1.1$ kpc (see also K. Kuijken & G. Gilmore 1989; G. Kordopatis et al. 2011). For example, for the thick disk, the midpoint of the adopted vertical interval, $|Z| = 2.5$ kpc, corresponds to $K_Z = 2.82$ (km s^{-1})^2 pc^{-1}. Thus, a single representative K_Z value was adopted for each vertical interval in the scale-height calculation.

This K_Z prescription was adopted to follow the Jeans-equation implementation used in previous scale-height analyses (e.g., G. Kordopatis et al. 2011), rather than being derived from the `MWPotential2014` model employed for the orbit integrations. We note that this choice introduces an explicit dependence of the inferred h_Z values on the adopted vertical-force model. This procedure allows each Galactic population to be characterized using dynamical parameters appropriate for its typical orbital distribution. The calculated velocity gradients ($\partial\sigma_{V_Z}/\partial Z$) and K_Z values for the thin- and thick-disk components are included in Table 5.

We emphasize that the scale heights inferred from Equation (15) are conditional on the adopted Galactic vertical force. In particular, the $K_Z/\sigma^2_{V_Z}$ term provides a substantial contribution to $1/h_Z$ for our sample, so that the resulting scale heights should not be interpreted as purely model-independent measurements. Their values also depend on the adopted sample selection through both σ_{VZ} and its vertical gradient.

For the thin-disk sample selected solely according to its present-day spatial distribution ($|Z| < 800$ pc), the scale height and radial scale length are $h_Z = 229$ pc and $h_R = 3.49$ kpc, respectively. Applying the kinematic population criterion ($TD/D \leqslant 1$) reduces the scale height to 147 pc while yielding a comparable radial scale length of 3.29 kpc. The smallest thin-disk scale height is obtained for the orbital selection based on $Z_{\max}$, resulting in $h_Z = 123$ pc and $h_R = 3.22$ kpc. In contrast, the thick-disk ($1 < Z_{\max} \leqslant 4$ kpc) population exhibits a substantially larger scale height of $h_Z = 865$ pc, whereas its radial scale length remains comparatively similar ($h_R = 2.97$ kpc). The derived radial scale lengths and vertical scale heights for all populations are included in Table 5. The relatively small variation in the radial scale length indicates that the principal structural difference between the two Galactic disk components lies in their vertical distribution rather than their radial extent. The orbital classification based on $Z_{\max}$ yields the smallest thin-disk scale height, suggesting that orbital parameters provide a more effective separation of thin- and thick-disk stars than either present-day positions or purely kinematic probability criteria.

5. Discussion

5.1. Thin-disk, Thick-disk, and Halo Velocity Dispersions

Table 6 presents the velocity dispersions for the thin-disk, thick-disk, and halo WDs in our sample along with representative values reported in the literature. Thin-disk WDs exhibit remarkably consistent velocity dispersions regardless of the adopted population criteria used ($S_{\rm tot}$, TD/D, or $Z_{\max}$). The derived values range from $(\sigma_U, \sigma_V, \sigma_W) = (32 \pm 3, 22 \pm 3, 20 \pm 3)$ km s^{-1} for the $S_{\rm tot}$ selection to $(36 \pm 3, 25 \pm 3, 18 \pm 3)$ km s^{-1} for the $Z_{\max}$ selection. These measurements are in excellent agreement with previous studies of WDs (E.-M. Pauli et al. 2003; W. H. Elsanhoury et al. 2015), nearby thin-disk stars (C. Soubiran et al. 2003; T. Bensby et al. 2014), W UMa–type variables (S. Bilir et al. 2005), and cataclysmic variables (T. Ak et al. 2010, 2015; R. Canbay et al. 2025). The close agreement between these independent stellar populations shows that the Gaia-based WD sample reliably reproduces the kinematic properties of the thin disk.

As expected, the thick-disk population exhibits substantially larger velocity dispersions. The largest radial velocity dispersion is obtained from the $S_{\rm tot}$ criterion, reaching $\sigma_U = 75 \pm 3$ km s^{-1}, which is consistent with $\sigma_U = 79$ km s^{-1} reported for the SPY WD sample by E.-M. Pauli et al. (2003). The corresponding σ_V and σ_W values are likewise consistent with measurements for nearby thick-disk stars reported by M. Chiba & T. C. Beers (2000), C. Soubiran et al. (2003), and T. Bensby et al. (2014). The lower σ_U values derived from the probability-based and orbital classification methods are expected, since they use the complete kinematic or orbital properties rather than just the total space velocities, thereby reducing the contribution of objects with exceptionally large radial motions.

The halo subsamples display the largest velocity dispersions, reflecting the dynamically hottest Galactic population, though our results suffer from small number statistics. The halo WD sample identified through the total space velocity displays velocity dispersions of $(\sigma_U, \sigma_V, \sigma_W) = (132 \pm 23, 93 \pm 16, 120 \pm 21)$ km s^{-1}, which closely match

Table 5
Galactocentric Mean Velocity Components and Space-velocity Dispersions of the White Dwarf Subsamples Used in the Jeans Analysis

Sample	Population	N	$\langle V_R \rangle$	$\langle V_\phi \rangle$	$\langle V_Z \rangle$ (km s^{-1})	σ_{VR}	σ_{V_ϕ}	σ_{V_Z}	$\partial\sigma_{V_Z}/\partial Z$ (km s^{-1} kpc^{-1})	K_Z ((km s^{-1})^2 pc^{-1})	h_R (kpc)	h_Z (pc)
$\lvert Z\rvert < 800$ pc	Thin disk	5825	1.61	−208.01	1.52	38.19	27.66	24.33	13.47	1.93	3.49	229
$TD/D \leqslant 1$	Thin disk	5468	1.18	−209.70	−1.59	35.23	22.66	18.93	13.47	1.93	3.29	147
$0 < Z_{\max} \leqslant 1$ kpc	Thin disk	5408	1.47	−206.97	−1.58	36.39	25.33	17.73	21.39	1.93	3.22	123
$1 < Z_{\max} \leqslant 4$ kpc	Thick disk	412	3.89	−165.13	21.70	54.69	43.19	57.74	24.39	2.82	2.97	865

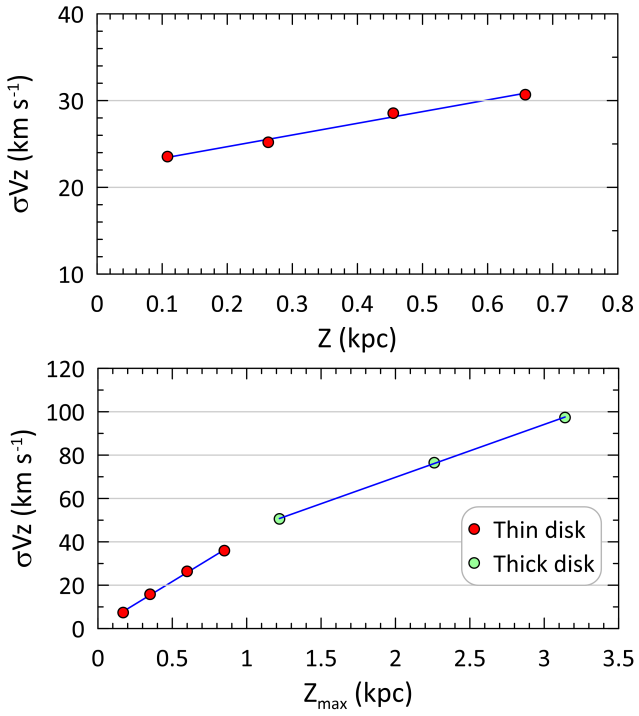


Figure 9. Velocity dispersion as a function of distance from the Galactic plane. The upper panel shows the present-day vertical distances (Z) of the WDs from the Galactic plane, while the lower panel shows their maximum vertical distances ($Z_{\max}$) reached along their Galactic orbits.

the values reported by M. Chiba & T. C. Beers (2000) and E.-M. Pauli et al. (2003) in σ_U and σ_V. The lower dispersions obtained from the probability-based classification most likely arise because of contamination from thick-disk objects.

All three classification methods recover the same fundamental kinematic sequence, namely a systematic increase in the velocity dispersions from the thin disk to the thick disk and finally to the halo. This behavior is fully consistent with the long-established picture of secular disk heating (R. Wielen 1977; B. Nordström et al. 2004; M. Aumer & J. J. Binney 2009), in which repeated gravitational interactions with molecular clouds, spiral arms, the Galactic bar, and external perturbations progressively increase stellar random motions over time (J. Binney & S. Tremaine 2008; J. A. Sellwood 2014; J. Bland-Hawthorn & O. Gerhard 2016).

5.2. The Guiding-radius Distributions

The guiding-radius distributions provide a useful dynamical comparison among the Galactic stellar populations because R_g is closely related to orbital angular momentum. The top panel in Figure 10 presents our results on the normalized R_g distributions for the thin disk, thick disk, and the halo. The distribution peaks at $R_g = 7.88$ kpc for the thin disk, 5.62 kpc for the thick disk, and 4.38 kpc for the halo, revealing the expected systematic decrease in characteristic orbital radius from dynamically cold to dynamically hot Galactic populations.

For comparison, we use the quantitative guiding-radius results reported by A. Zubiaur et al. (2024). Their sample is based on the Galactic population classifications of S. Torres et al. (2019), who used a random forest algorithm trained on synthetic thin-disk, thick-disk, and halo populations generated through population-synthesis modeling. Thus, the population assignments adopted by A. Zubiaur et al. (2024) are probabilistic rather than being based on fixed kinematic thresholds. Despite the different classification methodology from that adopted in the present work, the resulting R_g distributions show broadly similar characteristic trends. Specifically, A. Zubiaur et al. (2024) report mean guiding radii of approximately 7.9, 6.7, and 4.2 kpc for the thin-disk, thick-disk, and halo populations, respectively, providing a quantitative comparison with the values derived in the present study.

The nearly identical peak positions obtained for the thin-disk and halo populations demonstrate that the characteristic angular momenta of these populations are recovered consistently despite the use of different datasets and classification techniques. The modest offset of approximately 1 kpc for the thick disk is likely due to differences in sample selection, survey volume, and population assignment.

5.3. Galactic Structural Parameters

We used three independent classification schemes ($S_{\rm tot}$, TD/D, and $Z_{\max}$) to constrain the relative fractions of the Galactic populations. For the full sample of 5837 WDs, the three classification methods yield thin-disk fractions of 91%–94%, while the inferred thick-disk fraction varies more substantially between methods and the halo fraction remains below 1%. These fractions are broadly consistent with Galactic population studies based on nearby field stars and large photometric surveys (e.g., S. Karaali et al. 2003, 2004, 2007; A. C. Robin et al. 2003; S. Bilir et al. 2006a, 2006b, 2006c, 2008; S. Ak et al. 2007; M. Jurić et al. 2008; S. İyisan et al. 2025), confirming that the local WD population is overwhelmingly dominated by the thin disk.

The structural parameters were derived for three independently selected thin-disk samples and one thick-disk sample. The thin-disk scale height decreases systematically from $h_Z = 229$ pc for the purely spatial sample ($\lvert Z\rvert < 800$ pc) to 147 pc for the kinematically selected sample ($TD/D \leqslant 1$), reaching its minimum value of 123 pc for the orbitally selected sample ($Z_{\max} \leqslant 1$ kpc). In contrast, the radial scale length

Table 6
Thin-disk, Thick-disk, and Halo Velocity Dispersions

Source	N	σ_U	σ_V (km s^{-1})	σ_W	Population	Object
			Thin Disk			
E.-M. Pauli et al. (2003)	361	34	24	18	Thin disk	WDs
C. Soubiran et al. (2003)	⋯	39 ± 2	20 ± 2	20 ± 1	Thin disk	Solar neighborhood
S. Bilir et al. (2005)	129	36 ± 7	26 ± 7	19 ± 5	Thin disk	W Ursae Majoris
T. Ak et al. (2010)	131	29 ± 5	21 ± 4	17 ± 4	Thin disk	Cataclysmic variables
T. Bensby et al. (2014)	387	35	20	16	Thin disk	Solar neighborhood
T. Ak et al. (2015)	199	34 ± 4	28 ± 4	18 ± 4	Thin disk	Cataclysmic variables
W. H. Elsanhoury et al. (2015)	141	39	27	32	Thin disk	WDs
R. Canbay et al. (2025)	354	34 ± 3	24 ± 3	18 ± 2	Thin disk	Cataclysmic variables
This study ($S_{\rm LSR} \leqslant 80$ km s^{-1})	5304	32 ± 3	22 ± 3	20 ± 3	Thin disk	WDs
This study ($TD/D \leqslant 1$)	5468	35 ± 3	23 ± 3	19 ± 3	Thin disk	WDs
This study ($Z_{\rm max} \leqslant 1$ kpc)	5408	36 ± 3	25 ± 3	18 ± 3	Thin disk	WDs
			Thick Disk			
M. Chiba & T. C. Beers (2000)	⋯	46 ± 4	50 ± 4	35 ± 3	Thick disk	Solar neighborhood
E.-M. Pauli et al. (2003)	27	79	36	46	Thick disk	WDs
C. Soubiran et al. (2003)	⋯	63 ± 6	39 ± 4	39 ± 4	Thick disk	Solar neighborhood
T. Bensby et al. (2014)	203	67	38	35	Thick disk	Solar neighborhood
R. Canbay et al. (2025)	13	56 ± 2	50 ± 4	34 ± 2	Thick disk	Cataclysmic variables
This study ($80 < S_{\rm LSR} \leqslant 180$ km s^{-1})	516	75 ± 3	41 ± 3	46 ± 3	Thick disk	WDs
This study ($TD/D > 10$ and $TD/H > 1$)	186	71 ± 4	47 ± 2	67 ± 3	Thick disk	WDs
This study ($1 < Z_{\rm max} \leqslant 4$ kpc)	412	54 ± 3	43 ± 3	58 ± 3	Thick disk	WDs
			Halo			
M. Chiba & T. C. Beers (2000)	⋯	141 ± 11	106 ± 9	94 ± 8	Halo	Solar neighborhood
E.-M. Pauli et al. (2003)	7	138	95	47	Halo	WDs
T. Ak et al. (2010)	10	78 ± 4	63 ± 5	48 ± 5	Halo	Cataclysmic variables
T. Ak et al. (2015)	17	59 ± 3	50 ± 3	66 ± 4	Halo	Cataclysmic variables
T. Bensby et al. (2014)	36	160	90	90	Halo	Solar neighborhood
R. Canbay et al. (2025)	18	78 ± 2	75 ± 2	62 ± 3	Halo	Cataclysmic variables
This study ($S_{\rm LSR} > 180$ km s^{-1})	17	132 ± 23	93 ± 16	120 ± 21	Halo	WDs
This study ($TD/D > 10$ and $TD/H \leqslant 1$)	16	123 ± 22	103 ± 19	137 ± 25	Halo	WDs
This study ($Z_{\rm max} > 4$ kpc)	17	91 ± 16	100 ± 18	151 ± 27	Halo	WDs

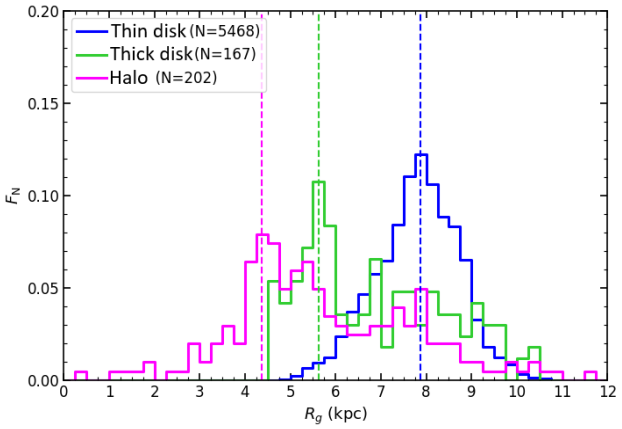


Figure 10. Normalized histograms of the $R_{\rm g}$ distributions for the Galactic populations identified in this study.

remains comparatively stable, varying between 3.22 and 3.49 kpc.

The derived structural parameters compare favorably with previous Galactic structure studies. Although the exact values depend on the adopted stellar tracers and selection criteria, virtually all investigations find a thin disk characterized by a relatively small vertical scale height and a significantly thicker disk component extending several hundred parsecs above the Galactic plane (A. C. Robin et al. 2003; M. Jurić et al. 2008; J. Bovy 2017). The comparatively small thin-disk scale height in this study likely reflects the orbital selection procedure, which efficiently removes stars with large vertical excursions, along with the relatively young progenitor population represented by many of the WDs. Conversely, the thick-disk scale height of 865 pc agrees remarkably well with the ∼900 pc value reported by M. Jurić et al. (2008), supporting the robustness of the present analysis. The radial scale lengths derived in this study are somewhat larger than those reported for main-sequence and red-clump stars (S. Bilir et al. 2006a; E. Yaz Gökçe et al. 2015). Such differences are expected because radial scale lengths depend on the adopted Galactic potential, sample selection, and the stellar tracer population.

5.4. Age–Velocity Dispersion Relation

The AVR provides one of the strongest observational constraints on the secular evolution of the Galactic disk. Stars are born with relatively small random motions that gradually increase through gravitational interactions with giant molecular clouds, transient spiral arms, the Galactic bar, and satellite perturbations (L. Spitzer & M. Schwarzschild 1951, 1953; R. Wielen 1977; J. A. Sellwood & J. J. Binney 2002; M. Aumer & J. J. Binney 2009). Consequently, older stellar populations exhibit systematically larger velocity dispersions than younger populations, making the AVR a powerful tracer of the dynamical heating history of the Milky Way.

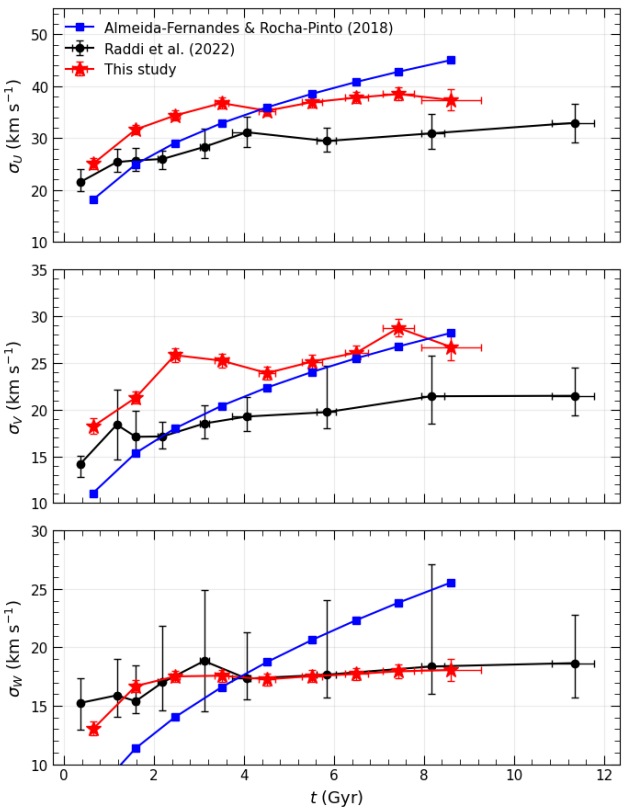


Figure 11. AVRs found in this study (red) vs. two other studies in the literature (black and blue points).

For our sample of WDs with reliable total ages, all three space-velocity components exhibit a clear increase in velocity dispersion with increasing stellar age. The same trend is recovered for both the full sample and the thin-disk subsamples selected using the $TD/D \leqslant 1$ and $Z_{\max} \leqslant 1$ kpc criteria, indicating that the observed AVR is not an artifact of the adopted population selection. The correlation becomes stronger for the dynamically homogeneous thin-disk samples, where contamination from thick-disk and halo stars is minimized, demonstrating that the secular dynamical heating of the Galactic disk is robustly detected in the WD population.

Figure 11 compares our results with those obtained from the WD sample of R. Raddi et al. (2022) and the main-sequence star sample of F. Almeida-Fernandes & H. J. Rocha-Pinto (2018). The overall increase in σ_U, σ_V, and σ_W with age is consistent among all three investigations, confirming the universal nature of the AVR. Our sample exhibits systematically larger σ_U and σ_V values than those reported by R. Raddi et al. (2022), though they are consistent with F. Almeida-Fernandes & H. J. Rocha-Pinto (2018) for ages older than 4 Gyr.

S. M. Arseneau et al. (2025) found systematic velocity differences of order 5–15 km s^{-1} between the SDSS spectra and higher-resolution SPY data. They found that the SDSS radial velocities tend to be higher than expected from the gravitational redshifts and provided corrections for the resolution-induced redshifts. However, repeating our entire analysis after including these corrections did not noticeably change the velocity dispersions shown in Figure 11. In any case, given the errors, the differences between our results and those of R. Raddi et al. (2022) are not statistically significant. Furthermore, the vertical velocity dispersion, σ_W, agrees remarkably well with R. Raddi et al. (2022) measurements over the entire age range. Beyond $\sim$4 Gyr, the three independent studies converge toward nearly identical velocity dispersions, suggesting that the long-term dynamical evolution of the Galactic disk dominates over differences in stellar tracers and analysis techniques.

5.5. Radial Migration and Orbital Blurring

To study the impact of radial migration and orbital blurring on our WD sample, we divide the sample into thin-disk, thick-disk, and halo groups using the total space-velocity criteria of P. E. Nissen (2004). This is the same kinematic grouping used in Figure 7 and differs from the probability-based classification applied elsewhere in the paper. The inferred birth radii are based on backward orbit integrations and therefore depend on the adopted Galactic potential. The mean $|R_g - R_b|$ and $|R_{gc} - R_b|$ values are 0.55 ± 0.58 and 0.73 ± 0.83 kpc for the thin disk and 1.82 ± 1.42 and 1.57 ± 1.55 kpc for the thick disk, respectively. Thus, both displacement measures are larger in the thick-disk group. The binned thin-disk medians show a modest, nonmonotonic increase with age in $|R_g - R_b|$, whereas the thick-disk medians show no clear age trend. The substantial scatter cautions against interpreting individual displacements as direct measures of past dynamical interactions. Only 11 halo WDs have total-age estimates, preventing a reliable determination of an age trend or characteristic displacement for that group. The two disk displacement measures have comparable magnitudes, suggesting that the difference between the present guiding radius and the inferred birth radius is relevant to the radial distribution of both populations. However, because these quantities do not provide an additive decomposition of radial migration and orbital blurring, we do not assign separate fractional contributions to the two processes.

Although inward migrators outnumber outward migrators, the uneven spatial coverage of the SDSS sample may affect their observed ratio. The present data therefore do not establish a preferred migration direction for the Galactic disk. A spatially more complete WD sample is required to constrain the overall balance between inward and outward migration.

The radial-displacement trends found for the WD sample are broadly consistent with studies based on other stellar tracers. Bayesian reconstructions of stellar birth radii using APOGEE red giants show that many solar-neighborhood stars formed several kpc from their present locations (N. Frankel et al. 2018, 2020). Evidence for radial redistribution is also seen in red-clump stars (F. Anders et al. 2017), FGK disk stars (S. Sharma et al. 2021), open clusters (M. Netopil et al. 2022; R. Canbay et al. 2026; D. C. Çinar et al. 2026a, 2026b; T. Yontan et al. 2026), and APOGEE DR17 samples of main-sequence turnoff and subgiant branch stars (A. B. A. Queiroz et al. 2023). Taken together, these studies demonstrate that radial redistribution is an important aspect of Galactic disk evolution across a wide range of stellar tracers.

6. Conclusions and Future Prospects

We have presented a comprehensive kinematic and dynamical analysis of a sample of 5837 DA WDs constructed by combining SDSS DR19 spectroscopy (N. R. Crumpler et al. 2025) with Gaia DR3 astrometry (Gaia Collaboration

et al. 2023). High-precision Gaia astrometric measurements and homogeneous atmospheric parameters from the SDSS provide one of the largest and most reliable WD samples currently available for investigating the dynamical evolution of the Galactic disk.

The kinematic analysis shows that the sample is dominated by thin-disk WDs, while smaller fractions belong to the thick disk and halo. Independent population classifications based on total space velocity, the kinematic probability formalism of T. Bensby et al. (2003, 2005), and Galactic orbital parameters yield consistent results, demonstrating that the different approaches identify similar Galactic populations. In all classification schemes, velocity dispersions increase systematically from the thin disk to the halo, accompanied by a progressively larger rotational lag and increasing orbital eccentricities. These trends indicate the transition from dynamically cold stellar populations on nearly circular Galactic orbits to dynamically hotter populations characterized by larger random motions and more eccentric trajectories.

The availability of reliable total stellar ages allows the AVR to be examined over a wide range of Galactic ages. The velocity dispersions of all three velocity components increase systematically with age, with the strongest dependence observed in the radial component. The derived power-law indices are in good agreement with previous observational studies of Galactic disk stars, confirming that WDs preserve the dynamical signatures of long-term disk heating. Moreover, the comparison of $R_{\rm b}$, $R_{\rm g}$, and $R_{\rm gc}$ demonstrates that a significant fraction of the sample has experienced radial migration. The observed increase in radial displacement with stellar age further supports the view that long-term angular momentum redistribution has played a major role in shaping the present-day distribution of local WDs.

Depending on the adopted population-selection criteria, the inferred thin-disk scale height ranges from 123 to 229 pc, whereas the radial scale length remains relatively stable at 3.22–3.49 kpc. The smallest thin-disk scale height is obtained for the orbital selection based on $Z_{\rm max}$, suggesting that orbital parameters provide the most effective separation of thin- and thick-disk populations. In contrast, the thick disk exhibits a substantially larger scale height of approximately 865 pc, consistent with a dynamically older and vertically more extended Galactic component.

The results presented in this study demonstrate that WDs constitute powerful tracers of the dynamical evolution of the Galactic disk. Their well-constrained total ages, combined with precise astrometric data from Gaia, enable investigations of Galactic kinematics, AVR, orbital evolution, and radial migration over timescales inaccessible to most other stellar populations. The consistency of our results with previous studies based on main-sequence stars, red giants, and nearby WDs confirms that the evolutionary pathways inferred for the Galactic disk are largely independent of the stellar tracers employed.

Future Gaia data releases, together with large-scale spectroscopic surveys such as SDSS-V (J. A. Kollmeier et al. 2026), WEAVE (S. Jin et al. 2024), 4MOST (R. S. de Jong 2019), DESI (DESI Collaboration et al. 2026), and MOONS (M. Cirasuolo et al. 2020), will substantially improve the precision of astrometric, kinematic, and atmospheric parameters, allowing larger and more homogeneous WD samples to be explored (see for example L. L. Amorim et al. 2026; M. Kilic et al. 2026a, 2026b; A. Swan et al. 2026). Such advances will facilitate more detailed studies of Galactic dynamical heating, radial migration, and the role of stellar remnants in Galactic archeology.

Acknowledgments

We thank the anonymous referee for their insightful and constructive suggestions that significantly improved the paper. O.C. thanks the Scientific and Technological Research Council of Türkiye (TÜBITAK) for funding this research under the 2214-A research project at the University of Oklahoma, as part of his doctoral thesis. M.K. gratefully acknowledges support by the NSF under grant AST-2508429, and the NASA under grants 80NSSC24K0380 and 80NSSC24K0436.

Facilities: Gaia (Gaia Collaboration et al. 2016; 2023), SDSS (D. G. York et al. 2000).

Software: `ChatGPT` (OpenAI 2026), `galpy` (J. Bovy 2015), `Matplotlib` (J. D. Hunter 2007), `NumPy` (C. R. Harris et al. 2020), `wdwarfdate` (R. Kiman et al. 2022).

Appendix
Catalog Description

Table A1 describes the columns included in the catalog, providing their names, definitions, and relevant details to facilitate the interpretation and use of the catalog.

Table A1
Description of the Columns in the Catalog

Column	Units	Description
ID	⋯	Order number
gaia_dr3_source_id	⋯	Gaia DR3 source identifier
ruwe	⋯	Gaia RUWE
S/N	⋯	Spectrum SNR
binary_flag	⋯	Flag indicating whether the WD is a potential binary
α	deg	R.A.
δ	deg	Decl.
l	deg	Galactic longitude
b	deg	Galactic latitude
d	pc	Median geometric distance from C. A. L. Bailer-Jones et al. (2021)
$d_{\rm err}$	pc	Distance uncertainty
$\mu_\alpha \cos\delta$	mas yr^{-1}	Proper motion in R.A.
$(\mu_\alpha \cos\delta)_{\rm err}$	mas yr^{-1}	Uncertainty in proper motion in R.A.
μ_δ	mas yr^{-1}	Proper motion in decl.
$(\mu_\delta)_{\rm err}$	mas yr^{-1}	Uncertainty in proper motion in decl.
$V_{\rm rad}$	km s^{-1}	Gravitational-redshift-corrected radial velocity ($V_{\rm grav}$)
$(V_{\rm rad})_{\rm err}$	km s^{-1}	Uncertainty in radial velocity
$X_{\rm gc}$	pc	Galactocentric Cartesian X-coordinate
$Y_{\rm gc}$	pc	Galactocentric Cartesian Y-coordinate
$Z_{\rm gc}$	pc	Galactocentric Cartesian Z-coordinate
$U_{\rm LSR}$	km s^{-1}	Galactic space-velocity component $U_{\rm LSR}$
$U_{\rm err}$	km s^{-1}	Uncertainty in $U_{\rm LSR}$
$V_{\rm LSR}$	km s^{-1}	Galactic space-velocity component $V_{\rm LSR}$
$V_{\rm err}$	km s^{-1}	Uncertainty in $V_{\rm LSR}$
$W_{\rm LSR}$	km s^{-1}	Galactic space-velocity component $W_{\rm LSR}$
$W_{\rm err}$	km s^{-1}	Uncertainty in $W_{\rm LSR}$
$S_{\rm LSR}$	km s^{-1}	Total space velocity relative to the LSR
$S_{\rm err}$	km s^{-1}	Uncertainty in the total space velocity
V_R	km s^{-1}	Galactocentric radial velocity component
V_ϕ	km s^{-1}	

Table A1
(Continued)

Column	Units	Description
		Galactocentric azimuthal velocity component
V_Z	km s^{-1}	Galactocentric vertical velocity component
TD/D	⋯	Thick- to thin-disk probability ratio
$Z_{\max}$	kpc	Maximum distance from the Galactic plane
$R_{\rm apo}$	kpc	Apogalactic distance
$R_{\rm peri}$	kpc	Perigalactic distance
e	⋯	Orbital eccentricity
$P_{\rm orb}$	Myr	Galactic orbital period
$R_{\rm gc}$	kpc	Present-day Galactocentric distance
$R_{\rm g}$	kpc	Guiding-center radius
$R_{\rm b}$	kpc	Birth radius
$T_{\rm eff}$	K	Photometric effective temperature
$(T_{\rm eff})_{\rm err}$	K	Uncertainty in photometric effective temperature
$\log g$	cgs	Surface gravity
$(\log g)_{\rm err}$	cgs	Uncertainty in surface gravity
$t_{\rm tot}$	Gyr	Total WD age estimated with `wdwarfdate`
$(t_{\rm tot})_{-\rm err}$	Gyr	Lower 1σ confidence limit of the total age
$(t_{\rm tot})_{+\rm err}$	Gyr	Upper 1σ confidence limit of the total age
$M_{\rm i}$	$M_\odot$	Initial (progenitor) mass estimated with `wdwarfdate`
$(M_{\rm i})_{-\rm err}$	$M_\odot$	Lower 1σ confidence limit of the initial mass
$(M_{\rm i})_{+\rm err}$	$M_\odot$	Upper 1σ confidence limit of the initial mass
$M_{\rm f}$	$M_\odot$	Final WD mass estimated with `wdwarfdate`
$(M_{\rm f})_{-\rm err}$	$M_\odot$	Lower 1σ confidence limit of the final mass
$(M_{\rm f})_{+\rm err}$	$M_\odot$	Upper 1σ confidence limit of the final mass

(This table is available in its entirety in machine-readable form in the online article.)

ORCID iDs

Ozcan Caliskan https://orcid.org/0009-0003-5839-8007
Selçuk Bilir https://orcid.org/0000-0003-3510-1509
Mukremin Kilic https://orcid.org/0000-0001-6098-2235

References

Ak, S., Bilir, S., Karaali, S., & Buser, R. 2007, AN, 328, 169
Ak, T., Bilir, S., Ak, S., Coşkunoğlu,, K. B., & Eker, Z. 2010, NewA, 15, 491
Ak, T., Bilir, S., Özdönmez, A., et al. 2015, Ap&SS, 357, 72
Akbaba, F., Ak, T., Bilir, S., et al. 2024, AN, 345, e20240052
Almeida-Fernandes, F., & Rocha-Pinto, H. J. 2018, MNRAS, 476, 184
Althaus, L. G., Córsico, A. H., Isern, J., & García-Berro, E. 2010, A&ARv, 18, 471
Amorim, L. L., Costa Junior, W. N., Kepler, S. O., et al. 2026, arXiv:2607.00430
Anders, F., Chiappini, C., Minchev, I., et al. 2017, A&A, 600, A70
Anguiano, B., Rebassa-Mansergas, A., García-Berro, E., et al. 2017, MNRAS, 469, 2102
Antoja, T., Helmi, A., Romero-Gómez, M., et al. 2018, Natur, 561, 360
Arseneau, S. M., Hermes, J. J., Zakamska, N. L., et al. 2025, ApJ, 991, 190
Aumer, M., & Binney, J. J. 2009, MNRAS, 397, 1286
Bailer-Jones, C. A. L., Rybizki, J., Fouesneau, M., Demleitner, M., & Andrae, R. 2021, AJ, 161, 147
Bédard, A., Bergeron, P., Brassard, P., & Fontaine, G. 2020, ApJ, 901, 93
Bensby, T., Feltzing, S., & Lundström, I. 2003, A&A, 410, 527
Bensby, T., Feltzing, S., Lundstrüm, I., & Ilyin, I. 2005, A&A, 433, 185
Bensby, T., Feltzing, S., & Oey, M. S. 2014, A&A, 562, A71
Bilir, S., Cabrera-Lavers, A., Karaali, S., et al. 2008, PASA, 25, 69
Bilir, S., Karaali, S., Ak, S., et al. 2012, MNRAS, 421, 3362
Bilir, S., Karaali, S., Ak, S., Yaz, E., & Hamzaoğlu, E. 2006a, NewA, 12, 234
Bilir, S., Karaali, S., & Gilmore, G. 2006b, MNRAS, 366, 1295
Bilir, S., Karaali, S., Güver, T., Karataş, Y., & Ak, S. G. 2006c, AN, 327, 72
Bilir, S., Karataş, Y., Demircan, O., & Eker, Z. 2005, MNRAS, 357, 497
Binney, J., & Tremaine, S. 2008, Galactic Dynamics: Second Edition (Princeton Univ. Press)
Bland-Hawthorn, J., & Gerhard, O. 2016, ARA&A, 54, 529
Bovy, J. 2015, ApJS, 216, 29
Bovy, J. 2017, MNRAS, 470, 1360
Bovy, J., & Rix, H.-W. 2013, ApJ, 779, 115
Bovy, J., & Tremaine, S. 2012, ApJ, 756, 89
Buser, R., Rong, J., & Karaali, S. 1999, A&A, 348, 98
Canbay, R., Ak, T., Bilir, S., Soydugan, F., & Eker, Z. 2025, AJ, 169, 87
Canbay, R., Çinar, D. C., Çalışkan, Ö., et al. 2026, arXiv:2606.31714
Çinar, D. C., Bisht, D., Jiang, I.-G., Belwal, K., & Bilir, S. 2026a, AJ, 172, 236
Çinar, D. C., Bisht, D., Jiang, I.-G., et al. 2026b, AJ, 172, 140
Chen, B., Stoughton, C., Smith, J. A., et al. 2001, ApJ, 553, 184
Cheng, S., Cummings, J. D., & Ménard, B. 2019, ApJ, 886, 100
Chiba, M., & Beers, T. C. 2000, AJ, 119, 2843
Choi, J., Dotter, A., Conroy, C., et al. 2016, ApJ, 823, 102
Cirasuolo, M., Fairley, A., Rees, P., et al. 2020, Msngr, 180, 10
Coşkunoğlu, B., Ak, S., Bilir, S., et al. 2011, MNRAS, 412, 1237
Coşkunoğlu, B., Ak, S., Bilir, S., et al. 2012, MNRAS, 419, 2844
Crumpler, N. R., Chandra, V., Zakamska, N. L., et al. 2025, ApJ, 989, 24
Cummings, J. D., Kalirai, J. S., Tremblay, P.-E., Ramirez-Ruiz, E., & Choi, J. 2018, ApJ, 866, 21
de Jong, R. S. 2019, NatAs, 3, 574
De Simone, R., Wu, X., & Tremaine, S. 2004, MNRAS, 350, 627
DESI Collaboration, Abdul Karim, M., Adame, A. G., et al. 2026, AJ, 171, 285
Dotter, A. 2016, ApJS, 222, 8
Elsanhoury, W. H., Nouh, M. I., & Abdel-Rahman, H. I. 2015, RMxAA, 51, 199
ESA 1997, ESA SP-1200, Astrometric and photometric star catalogues derived from the ESAESA HIPPARCOS Space Astrometry Mission (ESA)
Falcon, R. E., Winget, D. E., Montgomery, M. H., & Williams, K. A. 2010, ApJ, 712, 585
Fontaine, G., Brassard, P., & Bergeron, P. 2001, PASP, 113, 409
Frankel, N., Rix, H.-W., Ting, Y.-S., Ness, M., & Hogg, D. W. 2018, ApJ, 865, 96
Frankel, N., Sanders, J., Ting, Y.-S., & Rix, H.-W. 2020, ApJ, 896, 15
Gaia Collaboration, Brown, A. G. A., Vallenari, A., et al. 2018, A&A, 616, A1
Gaia Collaboration, Brown, A. G. A., Vallenari, A., et al. 2021, A&A, 649, A1
Gaia Collaboration, Prusti, T., de Bruijne, J., H., J., et al. 2016, A&A, 595, A1
Gaia Collaboration, Vallenari, A., Brown, A. G. A., et al. 2023, A&A, 674, A1
Gentile Fusillo, N. P., Tremblay, P.-E., Gänsicke, B. T., et al. 2019, MNRAS, 482, 4570
Gilmore, G., Wyse, R. F. G., & Kuijken, K. 1989, ARA&A, 27, 555
Grand, R. J. J., Springel, V., Kawata, D., et al. 2016, MNRAS, 460, L94
Harris, C. R., Millman, K. J., van der Walt, S. J., et al. 2020, Natur, 585, 357
Helmi, A., Babusiaux, C., Koppelman, H. H., et al. 2018, Natur, 563, 85
Holmberg, J., Nordström, B., & Andersen, J. 2009, A&A, 501, 941
Hunter, J. D. 2007, CSE, 9, 90
İyisan, S., Bilir, S., Önal Taş, Ö., & Plevne, O. 2025, AJ, 169, 138
Jiménez-Esteban, F. M., Torres, S., Rebassa-Mansergas, A., et al. 2018, MNRAS, 480, 4505
Jin, S., Trager, S. C., Dalton, G. B., et al. 2024, MNRAS, 530, 2688
Johnson, D. R. H., & Soderblom, D. R. 1987, AJ, 93, 864
Joncour, I., Duchêne, G., & Moraux, E. 2017, A&A, 599, A14
Jurić, M., Ivezić, Ž., Brooks, A., et al. 2008, ApJ, 673, 864
Karaali, S., Ak, S. G., Bilir, S., Karataş, Y., & Gilmore, G. 2003, MNRAS, 343, 1013
Karaali, S., Bilir, S., & Hamzaoğlu, E. 2004, MNRAS, 355, 307
Karaali, S., Bilir, S., Yaz, E., Hamzaoğlu, E., & Buser, R. 2007, PASA, 24, 208
Karl, C. A., Napiwotzki, R., Heber, U., et al. 2005, A&A, 434, 637
Kepler, S. O., Koester, D., Pelisoli, I., Romero, A. D., & Ourique, G. 2021, MNRAS, 507, 4646
Kepler, S. O., Pelisoli, I., Koester, D., et al. 2019, MNRAS, 486, 2169
Kilic, M., Munn, J. A., Harris, H. C., et al. 2017, ApJ, 837, 162

Kilic, M., Bergeron, P., Moss, A., et al. 2026a, ApJ, 1000, 216
Kilic, M., Bergeron, P., Blouin, S., et al. 2026b, ApJ, 1006, 248
Kiman, R., Xu, S., Faherty, J. K., et al. 2022, AJ, 164, 62
Kollmeier, J. A., Rix, H.-W., Aerts, C., et al. 2026, AJ, 171, 52
Kordopatis, G., Recio-Blanco, A., de Laverny, P., et al. 2011, A&A, 535, A107
Kuijken, K., & Gilmore, G. 1989, MNRAS, 239, 605
Lacey, C. G. 1984, MNRAS, 208, 687
Liebert, J., Dahn, C. C., & Monet, D. G. 1988, ApJ, 332, 891
Mestel, L. 1952, MNRAS, 112, 583
Mihalas, D., & Binney, J. 1981, Galactic astronomy. Structure and kinematics (W. H. Freeman and Company)
Minchev, I., & Famaey, B. 2010, ApJ, 722, 112
Miyamoto, M., & Nagai, R. 1975, PASJ, 27, 533
Napiwotzki, R., Christlieb, N., Drechsel, H., et al. 2001, AN, 322, 411
Navarro, J. F., Frenk, C. S., & White, S. D. M. 1996, ApJ, 462, 563
Netopil, M., Oralhan, İ. A., Çakmak, H., Michel, R., & Karataş, Y. 2022, MNRAS, 509, 421
Nissen, P. E. 2004, in Origin and Evolution of the Elements, ed. A. McWilliam & M. Rauch (Carnegie Observatories), 154
Nordström, B., Mayor, M., Andersen, J., et al. 2004, A&A, 418, 989
OpenAI 2026, ChatGPT (GPT-5.5), https://chatgpt.com
Pauli, E.-M., Napiwotzki, R., Altmann, M., et al. 2003, A&A, 400, 877
Pauli, E.-M., Napiwotzki, R., Heber, U., Altmann, M., & Odenkirchen, M. 2006, A&A, 447, 173
Queiroz, A. B. A., Anders, F., Chiappini, C., et al. 2023, A&A, 673, A155
Raddi, R., Torres, S., Rebassa-Mansergas, A., et al. 2022, A&A, 658, A22
Robin, A. C., Reylé, C., Derrière, S., & Picaud, S. 2003, A&A, 409, 523
Romero, A. D., Campos, F., & Kepler, S. O. 2015, MNRAS, 450, 3708
Rowell, N., & Kilic, M. 2019, MNRAS, 484, 3544
Schönrich, R., & Binney, J. 2009, MNRAS, 399, 1145
Sellwood, J. A. 2014, RvMP, 86, 1
Sellwood, J. A., & Binney, J. J. 2002, MNRAS, 336, 785
Sharma, S., Hayden, M. R., Bland-Hawthorn, J., et al. 2021, MNRAS, 506, 1761
Soubiran, C., Bienaymé, O., & Siebert, A. 2003, A&A, 398, 141
Spitzer, L., Jr., & Schwarzschild, M. 1951, ApJ, 114, 385
Spitzer, L., Jr., & Schwarzschild, M. 1953, ApJ, 118, 106
Swan, A., Gänsicke, B. T., Izquierdo, P., et al. 2026, MNRAS,
Ting, Y.-S., & Rix, H.-W. 2019, ApJ, 878, 21
Torres, S., Cantero, C., Rebassa-Mansergas, A., et al. 2019, MNRAS, 485, 5573
Tremblay, P.-E., Kalirai, J. S., Soderblom, D. R., Cignoni, M., & Cummings, J. 2014, ApJ, 791, 92
Wielen, R. 1977, A&A, 60, 263
Winget, D. E., Hansen, C. J., Liebert, J., et al. 1987, ApJL, 315, L77
Yaz Gökçe, E., Karaali, S., Duran, Ş., et al. 2015, PASA, 32, e012
Yontan, T., Bilir, S., Çakmak, H., et al. 2026, AdSpR, 78, 8569
York, D. G., Adelman, J., Anderson, J. E., Jr., et al. 2000, AJ, 120, 1579
Zubiaur, A., Raddi, R., & Torres, S. 2024, A&A, 687, A286